

Research paper

Rare earth ions doped $K_2Ta_2O_6$ photocatalysts with enhanced UV-vis light activity

Anna Krukowska^a, Michał Jerzy Winiarski^b, Judyta Strychalska-Nowak^b, Tomasz Klimczuk^b, Wojciech Lisowski^c, Alicja Mikolajczyk^d, Henry P. Pinto^e, Tomasz Puzyń^d, Tomasz Grzyb^f, Adriana Zaleska-Medynska^{a,*}

^a Department of Environmental Technology, Faculty of Chemistry, University of Gdańsk, 80-308 Gdańsk, Poland

^b Department of Solid State Physics, Faculty of Applied Physics and Mathematics, Gdańsk University of Technology, 80-233 Gdańsk, Poland

^c Institute of Physical Chemistry, Polish Academy of Sciences, 01-224 Warsaw, Poland

^d Laboratory of Environmental Chemometrics, Faculty of Chemistry, University of Gdańsk, 80-308 Gdańsk, Poland

^e School of Physical Sciences and Nanotechnology, Yachay Tech University, 1000119 Urcuquí, Ecuador

^f Department of Rare Earths, Faculty of Chemistry, Adam Mickiewicz University, 60-780 Poznań, Poland

ARTICLE INFO

ABSTRACT

Keywords:

Pyrochlore $K_2Ta_2O_6$
Rare earth ion doping
UV-vis photocatalytic activity
Phenol/toluene degradation
 H_2 generation

Novel rare earth-doped $K_2Ta_2O_6$ ($RE-K_2Ta_2O_6$) photocatalysts were successfully synthesized by one-step hydrothermal method. The effect of dopant type ($RE = Y, Yb, Ho, Pr, Er$) and amount of rare earth precursor (2, 4, 8 and 10 mol%) on the physicochemical and photocatalytic properties of $RE-K_2Ta_2O_6$ have been investigated. All as-prepared materials were subsequently characterized by UV-vis diffuse reflectance spectroscopy (DRS), Brunauer-Emmett-Teller (BET) specific surface area measurement, scanning electron microscopy (SEM) with energy dispersive X-ray spectroscopy (EDS), powder X-ray diffraction (PXRD), X-ray photoelectron spectroscopy (XPS), Raman spectroscopy, mass magnetic susceptometry and photoluminescence (PL) emission spectroscopy. The photocatalytic activity under UV-vis light irradiation was estimated in phenol degradation in aqueous phase, toluene removal in gas phase and H_2 generation from formic acid solution. The experimental results show that, novel $RE-K_2Ta_2O_6$ exhibits greatly improved degradation efficiency under UV-vis light irradiation compared with pristine $K_2Ta_2O_6$. The $Er-K_2Ta_2O_6$ and $Pr-K_2Ta_2O_6$, obtained by introducing of 2 mol% of RE ions during synthesis, reveal the highest photocatalytic activity among prepared samples in aqueous phase (33% of phenol decomposition after 90 min of irradiation) and gas phase (45% of toluene removal after 60 min of irradiation), respectively. Moreover, both photocatalysts present good stability after subsequent three cycles. The active species trapping test shows that $\cdot OH$ and $O_2\cdot^-$ radicals are significantly involved in phenol oxidation under UV-vis light irradiation. The amount of H_2 evolution increases with increasing addition of Er dopant into $K_2Ta_2O_6$ lattice. The highest H_2 production is obtained for 10 mol% $Er-K_2Ta_2O_6$ after 240 min of UV-vis light irradiation (15.40 $\mu\text{mol}/\text{min}$). Enhanced photoactivity performance can be attributed to incorporation of RE ions at K^+ lattice site in $RE-K_2Ta_2O_6$, probably leading to formation of new RE 4f states below the conduction band of $K_2Ta_2O_6$ structure. To investigate the localization of RE ions in $K_2Ta_2O_6$ structure, the band structure and partial density of the states (PDOS) have been investigated. Computer simulations were performed using plane-wave based Vienna *ab initio* simulation package (VASP) with the generalized gradient approximation (GGA) by Perdew-Burke-Ernzerhof (PBE). Moreover, inclusion of RE ions in $K_2Ta_2O_6$ causes predominance pyrochlore phase formation over perovskite in regular cubic structure. Summarized, RE -doped $K_2Ta_2O_6$ is promising material in photocatalytic degradation of organic pollutants and H_2 generation processes. Our work may provide valuable information for rare earth doping semiconductor with improved photocatalytic performance.

1. Introduction

Heterogeneous photocatalysis has been considered as the most promising novel process to solve the energy and environmental

pollution problems in highly selective and eco-friendly route. Photocatalytic semiconductors are able to transform toxic organic pollutants into CO_2 and H_2O as well as to produce clean and sustainable H_2 energy. Hence, photocatalysts are encouraging materials for various

* Corresponding author.

E-mail address: adriana.zaleska@ug.edu.pl (A. Zaleska-Medynska).

applications, such as: self-cleaning surfaces [1], wastewater and air purification [2], bacteria inactivation [3] and H₂ generation [4]. However, flaws like poor solar efficiency and equivocal photocatalytic mechanism for current semiconductor hinder its implementation at an industrial scale. Therefore, design and preparation of enhanced photocatalysts is an important issue and the greatest challenge at the present time.

The pyrochlore (K₂Ta₂O₆) and perovskite (KTaO₃) phases of potassium tantalate make its a functional photocatalytic material due to stability against thermal conditions, chemical and humidity, optical isotropy and high refractive index (2.2), excellent dielectric permittivity and low dielectric losses, high sensitivity and variability on doping [5]. The one-step hydrothermal/solvothermal synthesis of pristine potassium tantalate powder seems to be preferable preparation route due to well-controlled structure, morphology and particle size of final product. The pyrochlore phase is formed at lower KOH concentration [6], whereas more concentrated KOH solutions (> 15 mol/l) and higher temperature (> 190 °C) lead to perovskite phase formation [7]. Also the ratio of inert solvent (ethanol or hexane) to active solvent (water) plays the effect on crystalline behavior of potassium tantalate [8,9]. Tantalate exhibits a superb photocatalytic performance, because of its conduction band consisting of Ta 5d orbital located at a more negative position than the general catalysts such as titanate (Ti 3d) and niobate (Nb 4d) [10]. However, it cannot use efficiently the visible (vis) light of the solar energy because of its comparably wide band gap of about 4.5 and 3.4 eV for K₂Ta₂O₆ and KTaO₃, respectively [11]. Wang et al. estimated the band gap of tungsten bronze phase of potassium tantalate (K₆Ta_{10.8}O₃₀) of about 3.76 eV. The ultraviolet-induced photocatalytic property of K₆Ta_{10.8}O₃₀ is explained by presence of K⁺ in structure, which enhanced the electron transferring to O₂ and eliminated electron accumulation on K₆Ta_{10.8}O₃₀, leading increased separation of photogenerated electron-hole pairs [12]. Therefore, potassium tantalate is modified to improve photocatalytic activity by doping with: nitrogen (K₂Ta₂O_{6-x}N_x) [13], calcium or barium (Ca- or Ba-doped KTaO₃) [14], copper and vanadium (KTaO₃:Cu, V) [15], lanthanum (K_{1-x}La_xTaO₃) [16] and various metals (Zn²⁺, Y³⁺, Al³⁺, Ga³⁺, In³⁺, Ti⁴⁺, Zr⁴⁺, Hf⁴⁺, Si⁴⁺, Ge⁴⁺, Nb⁵⁺, Sb⁵⁺ or W⁶⁺ doped KTaO₃) [17]. As for example, Zhu et al. prepared in two-steps visible-light driven K₂Ta₂O_{6-x}N_x from N-doped Ta₂O₅ precursor and KOH solution by hydrothermal method [13]. In attempt to improved solar photocatalytic activity of KTaO₃, Paulauskas et al. introduced Ca or Ba doping in KTaO₃ [14]. Rossella et al. found out that, in KTaO₃ copper ions were inclusion at Ta⁵⁺ lattice site in two difference charge states Cu²⁺ and Cu⁺ causing charge compensated by oxygen vacancies [15]. In different study of KTaO₃ photocatalyst, Liu et al. incorporated La³⁺ at K⁺ lattice site, which reduced particle size causing enhanced separation of photogenerated electron-hole pairs [16]. Ishihara et al. compared the photocatalytic performance of different metal ions doped KTaO₃ towards H₂ generation in water splitting and found out that, trivalent metal ion dopant was the most efficient [17]. Also synthesis of composite material with heterojunction structure as hybrid of two semiconductor systems with matching band potentials have been reported. As for example, Gan et al. fabricated Bi₂O₂CO₃/Bi₃NbO₇ composite as an effective photocatalyst for inactivation of *Escherichia coli* in water under vis light irradiation. The formation of Bi₂O₂CO₃/Bi₃NbO₇ composite exhibited improved vis-induced bactericidal property due to efficient photogenerated electron-hole pairs separation at the interfaces of two semiconductors [18]. Although a few theoretical studies have been performed on undoped and doped KTaO₃, detailed investigation of effect of different dopant elements in K₂Ta₂O₆ and KTaO₃ is yet to be explored [19–21].

Rare earth (RE) doping tantalate-based semiconductor have shown significant advantages in photocatalytic applications in reduction of CO₂ into useful carbons [22,23], degradation of dye molecules [24–26] and generation of H₂ [27–34]. The RE group includes 15 lanthanide elements (La, Ce, Pr, Nd, Pm Sm, Eu, Gd, Tb, Dy, Ho, Er, Tm, Yb and Lu)

as well as scandium (Sc) and yttrium (Y), which exhibit mainly at +3 oxidation state. The incorporation of RE ions at A⁺ lattice site in ABO₃ (perovskite structure) causes interactions between empty and filled RE 4f states and photoexcited electron-hole pairs generated under UV-vis light irradiation affected on photocatalytic activity. The position of RE 4f levels in the electronic structure becomes monotonically lowered across the series of RE ions with increasing the number of 4f electrons. However, empty La 4f states is supposed to be higher than the conduction band (CB) edge, whereas Ce and Pr 4f levels are likely situated below the CB edge. The highest photocatalytic activity is attained by La doping due to overlap between Ta 5d and O 2p orbitals, which produces a wide density of the states distribution in the CB. Doping with the rest RE ions is also supposed to be active, because RE 4f states are located on or below the CB edge and play role as trapping center for photoexcited electrons. Therefore, RE-doped photocatalysts can be used to improve photocatalytic performance [35]. For instance, Jeyalakshmi et al. obtained maximum photocatalytic reduction of CO₂ in alkaline medium under UV-vis light irradiation for Na_(1-x)La_xTaO_(3+x) with NiO as co-catalyst [22] and Na_(1-x)La_xTaO_(3+x) in conjunction with cobalt tetra phenyl porphyrin [23]. La doping increased the crystallinity and induced level step sites on the surface. Moreover, the CB energy level became more negative and retarded charge carrier recombination. RE-doped alkali tantalate photocatalysts were also used in decomposition of dye molecules under UV light irradiation (safranine T by NaTaO₃:La obtained in hydrothermal treatment [24], methylene blue by Sm-NaTaO₃ synthesized in sol-gel method [25] and Rhodamine B by Na-TaO₃:La prepared under air, O₂ or H₂/Ar atmospheres in solid state reaction [26]). Furthermore, the H₂ generation has been extensively explored in processes from water splitting and from aqueous methanol solution. Kudo and Kato investigated the effect of lanthanide (La, Pr, Nd, Sm, Eu, Gd, Tb, Dy and Yb) doping into NiO/NaTaO₃ photocatalysts in water splitting. The photocatalytic activity were decreased when Eu and Yb ions were doped into NiO/NaTaO₃. The loaded NiO co-catalyst worked as a H₂ evolution site, indicating that photogenerated electrons had to reach the NiO surface [27]. Li et al. reported enhanced H₂ production from water splitting using visible-light driven photocatalyst (Er³⁺:YAlO₃/Pt-NaTaO₃) with Er³⁺:YAlO₃ as up-conversion luminescence agent [28]. Jana et al. synthesized Pt/RE:NaTaO₃ (RE = Y, La, Ce, Yb) catalysts in solid state reaction for the H₂ production in water splitting. Doping Y³⁺, La³⁺ or Yb³⁺ into Pt/RE:NaTaO₃ improved amount of evolved H₂, while Ce-doped sample exhibited lower activity than undoped catalyst [29]. Iwase, Kato und Kudo presented improved photocatalytic water splitting over Au/Na-TaO₃:La nanoparticles, where loaded Au co-catalyst was prepared by impregnation and photodeposition method, worked as H₂ evolution sites [30]. Torres-Martinez et al. demonstrated RuO₂/La:NaTaO₃ photocatalysts, where La doping created ordered surface nanostructure and RuO₂ acted role of electron trap in water splitting induced by UV light [31]. Husin et al. presented an innovative synthesis of La-doped NaTaO₃ [32] and nickel-loaded La_xNa_{1-x}TaO₃ [33] in H₂O₂-assisted sol-gel route, where La³⁺ occupied at Na⁺ lattice site. The La doping contributed to facilitate charge separation at surface reaction sites and suppress the recombination of photogenerated electron-hole pairs effectively in H₂ evolution from aqueous methanol solution under UV light irradiation. Additionally, La doped alkali tantalate photocatalysts were used in photocatalytic reforming of glucose for H₂ production [34]. Thus, the ability to modify properties of alkali tantalates by RE doping for enhanced photocatalytic performance is important for fabrication advanced functional photomaterials.

In view of above mentioned aspects, a series of novel RE-doped K₂Ta₂O₆ photocatalysts were prepared via one-step hydrothermal method. For the first time, in this work, the influence of a dopant type and amount of rare earth precursor on physicochemical properties of RE-K₂Ta₂O₆ (e.g. morphology, surface elemental composition, crystalline structure, magnetic, absorbance and photoluminescence attributes) were investigated and correlated with photocatalytic performance. The

photocatalytic activity and stability of as-prepared samples under UV-vis light irradiation were examined in the three model reactions: phenol degradation in the aqueous phase, toluene removal in the gas phase and H₂ generation from formic acid solution. A possible mechanism discussion for the generation of a reactive oxygen species in phenol oxidation and H₂ production from formic acid solution under UV-vis light irradiation were presented as well. To the best of our knowledge, complementary experimental and theoretical studies including band structure and partial density of the states (PDOS) of selective RE-K₂Ta₂O₆ (RE = Y, Yb, Ho, Pr, Er) powders have not been yet reported in literature.

2. Experimental

2.1. Materials and instruments

Tantalum(V) oxide (> 99% purity) from Sigma-Aldrich (Germany) and KOH (pure p.a.) from Chempur (Poland) were used as precursors for the synthesis of K₂Ta₂O₆ powder. Y(NO₃)₃·6H₂O (99.99%), Yb(NO₃)₃·5H₂O (99.9%), Ho(NO₃)₃·5H₂O (99.99%), Pr(NO₃)₃·6H₂O (99.9%) and Er(NO₃)₃·5H₂O (99.9%) salts from Sigma-Aldrich (Germany) were used as rare earth source in the preparation procedure of RE-doped K₂Ta₂O₆. Anhydrous ethanol (99.8%) and polyethylene glycol 400 (PEG-400) were purchased from POCh S.A. (Poland). Phenol (pure p.a.), toluene (99.8%) and formic acid (85%) from POCh S.A. (Poland) were used in photocatalytic performance. Coumarin (98%) from Sigma-Aldrich (Germany) was used in hydroxyl radical test. Ammonium oxalate (99.5%), silver nitrate (99%), *p*-benzoquinone (98%) and *tert*-butyl alcohol (99.5%) were purchased from Sigma-Aldrich (Germany) and used as scavengers. All the chemicals were used as received without further purification. Deionized water was used for all reactions and treatment processes.

Diffuse reflectance spectra (DRS) were characterized by Thermo Scientific Evolution 220 UV-vis spectrophotometer equipped with ISA-220 integrating sphere accessory. The DRS UV-vis spectra were recorded in the range of 250–750 nm using a BaSO₄ as the reference. The absorption spectra were converted from DRS UV-vis data by Kubelka-Munk function. Nitrogen adsorption-desorption isotherms at –196 °C were measured by a Micromeritics Gemini V model 2365 physisorption analyzer. The specific surface areas were determined by Brunauer–Emmett–Teller (BET) method in the relative pressure (p/p₀) range of 0.05–0.3. Also pore volumes were investigated. Previous to nitrogen adsorption surveys, all the samples were degassed under vacuum at 200 °C for 2 h. The morphology of the synthesized material was investigated using FEI Quanta 250 FEG scanning electron microscope (SEM) under high vacuum mode with accelerating voltage 30 kV. Energy-dispersive X-ray spectroscopy (EDS) measurements were carried out using SEM-integrated EDAX Apollo-X SDD detector with EDAX TEAM software and eZAF quantization method. Powder X-ray diffraction (PXRD) patterns were conducted on Philips X'Pert Pro MPD Philips diffractometer with Cu K_α radiation ($\lambda = 1.5418 \text{ \AA}$) in the 2θ range of 10–70°. The results were processed by means of LeBail analysis using High Score Plus software and crystallite size was estimated by Scherrer equation. X-ray photoelectron spectroscopy (XPS) measurements were performed using the a PHI 5000 VersaProbe (ULVAC-PHI) spectrometer with monochromatic Al K_α radiation ($h\nu = 1486.6 \text{ eV}$) from an X-ray source operating at 100 μm spot size, 25 W and 15 kV. The high-resolution (HR) XPS spectra were collected with the hemispherical analyzer at the pass energy of 23.5 eV and the energy step size of 0.1 eV and the photoelectron take off angle 45° with respect to the surface plane. The CasaXPS software (version 2.3.16) was used to evaluate the XPS data. Deconvolution of all HR XPS spectra were performed using a Shirley background and a Gaussian peak shape with 30% Lorentzian character. The binding energy (BE) scale of all detected spectra was referenced by setting the BE of the aliphatic carbon peak (C–C) signal to 285.0 eV. Raman spectroscopy was determined by Brucker Optics

model IFS 66 spectrometer with 260 nm laser at the excitation source. Raman spectra were recorded in the range of 100–1000 cm^{−1}. Mass magnetic susceptibility was measured using Physical Property Measurement System (Quantum Desing) with ACMS option under applied magnetic field of 1 T in the temperature range of 2–300 K. The photoluminescence (PL) spectroscopy was characterized by Perkin-Elmer 50 B luminescence spectrophotometer equipped with Xe discharge lamp as an excitation source and R928 photomultiplier as a detector, obtained at room temperature (293 K). PL spectra of synthesized material was excited by Xe lamp light with 325 nm wavelength and were scanned between 350 and 750 nm. PL spectra were corrected for the instrumental response.

2.2. Preparation of RE-K₂Ta₂O₆ photocatalysts

The hydrothermal method was used for the synthesis of RE-K₂Ta₂O₆ based on previously published procedures of production potassium tantalate [6,8,9]. In a preparation process, KOH (12 g) was dissolved in deionized H₂O (24 ml), then Ta₂O₅ (4.4 g) and PEG-400 (1.2 ml) were added to the solution. The appropriate amount of rare earth precursor was dissolved in deionized H₂O (2 ml) and introduced to the suspension. The molar ratios of selected rare earth metal to K₂Ta₂O₆ were 2 and 4 mol% (in addition 8 and 10 mol% for Er dopant). The mixture was stirred for 1 h to obtain homogeneous suspension, before it was transferred into a Teflon-lined stainless steel autoclave (V = 200 ml). The autoclave was sealed and heated at 190 °C for 24 h. After being cooled in the air to room temperature, the precipitates were washed several times by distilled H₂O with addition of C₂H₅OH and dried in an oven at 60 °C for 10 h. The desired white RE-K₂Ta₂O₆ powder was obtained. Pristine K₂Ta₂O₆ was synthesized using the same preparation process as the reference sample.

2.3. Theoretical calculations

Calculations were performed using the plane-wave based Vienna *ab initio* simulation package (VASP) [36–38] with the generalized gradient approximation (GGA) by Perdew-Burke-Ernzerhof (PBE) [39]. The valence states involved for the construction of the potential are K 3p⁶4s¹, Ta 6s²5d³, O 2s²2p⁴, Er 5p⁶5s²4f¹²6s², Pr 5p⁶5s²4f³6s² and were described by projector augmented wave potential (PAW) [40–42]. Simulations were performed with a cut-off energy of 550 eV and a Γ centered Monkhorst-Pack grid with a k-point separation of 0.028 Å^{−1} and 0.035 Å^{−1} for K₂Ta₂O₆ and KTaO₃ systems, respectively, which corresponds to a k-point mesh of 6 × 6 × 6 (7 × 7 × 7) for primitive cell of K₂Ta₂O₆ (KTaO₃) and 3 × 3 × 3 (4 × 4 × 4) for RE-doped K₂Ta₂O₆ (RE-doped KTaO₃) supercells, respectively. Using those parameters, we converged the total energy to < 1 meV/atom. Moreover, all the structures considered in this study were fully relaxed until all of the forces were < 0.02 eV Å^{−1}. The computed optimal lattice parameters were a = b = c = 10.699 Å for bulk K₂Ta₂O₆, and a = b = c = 4.033 Å for bulk KTaO₃ structures. The doped systems have been modeled with 1 × 1 × 1 supercell (80 atoms) of the cubic RE-K₂Ta₂O₆ crystal structure and with 2 × 2 × 2 supercell (40 atoms) of the cubic RE-KTaO₃ crystal structure. In our models, one K⁺ in the supercell was replaced by one Er³⁺/Pr³⁺ to generate Er-K₂Ta₂O₆, Pr-K₂Ta₂O₆, Er-KTaO₃ and Pr-KTaO₃ systems.

2.4. Measurement of photocatalytic activity in the aqueous phase

The photoactivity under UV-vis light irradiation of obtained samples was estimated by measuring the phenol decomposition in aqueous solution. Phenol was selected as a model water contaminant, because it is non-volatile and common pollutant in industrial wastewaters. The aqueous phase containing the photocatalyst (7.5 mg) and phenol solution (15 ml, C = 20 mg/l) was suspended in pyrex tubes (V = 20 ml). The temperature of the liquid phase during the process was maintained

at $10 \pm 0.5^\circ\text{C}$ by thermostatically controlled water bath. The prepared suspension was magnetic stirred for 30 min in the dark to reach the adsorption-desorption equilibrium. A reference measurement was taken just before starting irradiation. After that, the content of the tubes was photoirradiated with a 150 W Hg medium pressure lamp (Heraeus Noblelight GmbH), which emitted UV-vis light irradiation. The optical path included a filter of pyrex tubes ($\lambda \geq 270\text{ nm}$). Measured light flux was 6 mW/cm^2 (Hamamatsu UV Power meter). The suspension (1 ml) was collected at regular time periods of 30 min during 90 min of irradiation, then filtered through syringe filters ($\varnothing = 0.2\text{ }\mu\text{m}$) to remove the photocatalyst particles. Phenol concentration was estimated by colorimetric method ($\lambda = 480\text{ nm}$) after derivatization with diazo-*p*-nitroaniline using UV-vis spectrophotometer (Thermo Scientific Evolution 220). The photocatalytic phenol degradation was established by blind tests in the absence of photocatalyst or illumination, where no significant degradation of phenol was observed.

Additionally, the photoactivity under vis light irradiation of as-prepared samples was also estimated by measuring the phenol degradation in aqueous solution. The experiment was conducted in similar conditions as phenol decomposition under UV-vis light irradiation, expect below mentioned aspects. The aqueous phase containing the photocatalyst (125 mg) and phenol solution (25 ml, C = 20 mg/l) was placed in a photoreactor (V = 25 ml) equipped with quartz window. The prepared suspension was aerated ($6\text{ dm}^3/\text{h}$). The content of the reactor was photoirradiated with a 1000 W Xe lamp (Oriel), which emitted both UV and vis light irradiation. The optical path included a water filter and glass filter (GG420, Optel) to cut off wavelengths shorter than 420 nm, which measured light flux was 5 mW/cm^2 . The photocatalytic phenol degradation was also established by blind tests in the absence of photocatalyst or illumination, where no significant degradation of phenol was observed.

2.5. Measurement of photocatalytic activity in the gas phase

The photoactivity of prepared samples was also determined in gaseous toluene degradation process. Toluene was selected as a model gas contaminant in air purification from volatile organic compounds (VOC). The toluene removal in gas phase was performed in flat stainless steel reactor (V = 30 cm³) equipped with septa, valves and quartz window. As an irradiation source was used array of 5 UV ($\lambda_{\max} = 375\text{ nm}$) and 20 vis ($\lambda_{\max} = 415\text{ nm}$) light-emitting diodes (LEDs). Measured light flux was 0.35 mW/cm^2 . Photocatalyst powder (0.2 g) was suspended in small amount of water, loaded as thin layer on glass plate (20 mm x 20 mm) and dried. Then obtained plate coated with photocatalyst was placed at the bottom side of the reactor, followed by closing the reactor with quartz window. The gaseous mixture was passed through the reactor space for 1 min. The concentration of toluene in gaseous mixture was 200 ppm. After closed valves, the reactor was kept in dark for 30 min to reach the adsorption-desorption equilibrium. A reference measurement was taken just before starting irradiation. After that, the toluene content was estimated at regular time periods of 10 min during 60 min of irradiation. The analysis of toluene concentration in the gas phase was performed using Perkin Elmer Clarus 500 gas chromatograph equipped with Elite-5 capillary column (30 m x 0.25 mm, 0.25 μm) and flame ionization detector (FID) with He as a carrier gas. The measured samples were injected using a gas-tight syringe (V = 200 μl). The photocatalytic stability of all as-prepared samples was estimated in two subsequent cycles of toluene degradation process under UV-vis LEDs light irradiation. The photocatalytic toluene degradation was established by blind tests in the absence of a photocatalyst or illumination, where toluene loss was not significant observed.

2.6. Measurement of the photocatalytic H₂ generation

The photoactivity of obtained samples was also examined for H₂

production in the presence of formic acid solution. Addition of organic compound can be the efficient source of electron donors in photocatalytic H₂ generation. The H₂ evolution was performed in closed quartz reactor (V = 110 ml), where photocatalyst powder (0.2 g) was dispersed in aqueous formic acid solution (80 ml, C = 10%). The temperature of the aqueous phase during the process was maintained at $10 \pm 0.5^\circ\text{C}$ by thermostatically controlled water bath. As an irradiation source was used 250 W Xe lamp (Heraeus Noblelight GmbH), which emitted UV-vis light irradiation. Measured light flux was 60 mW/cm^2 . After tightly closed reactor, the prepared suspension was magnetic stirred for 30 min. During that time, nitrogen was bubbled ($8\text{ dm}^3/\text{h}$) through the reaction mixture to remove the oxygen content. A reference measurement was taken just before starting irradiation. Then the amount of evolved H₂ was determined at regular time periods of 30 min during 240 min of irradiation using a Perkin Elmer Clarus 500 gas chromatograph equipped with HayeSep Q (80/100) column and thermal conductivity detector (TCD) with N₂ as a carrier gas. The measured samples were dosed using a gas-tight syringe (V = 200 μl). The H₂ generation was established by blind test in the absence of a photocatalyst, where evolution of H₂ was not observed.

2.7. Measurement of formation hydroxyl radicals and active species trapping

The formation of hydroxyl radicals ($\cdot\text{OH}$) in the presence of pristine K₂Ta₂O₆ and RE-K₂Ta₂O₆ photocatalysts under UV-vis light irradiation was evaluated by fluorescence (FL) spectroscopy using coumarin as trapping agent. Detected fluorescent 7-hydroxycoumarin was produced in reaction of coumarin with $\cdot\text{OH}$ radical. The generation of $\cdot\text{OH}$ radicals during photocatalytic reaction was estimated using the same experimental set-up as for measuring efficiency of phenol degradation under UV-vis light irradiation. The experiment was performed in pyrex tubes containing photocatalyst (15 mg) and coumarin aqueous solution (15 ml, C = 0.15 g/l). The suspension (2 ml) was collected at regular time periods of 30 min during 90 min of irradiation, then filtered through syringe filters ($\varnothing = 0.2\text{ }\mu\text{m}$) to remove the photocatalyst particles. The filtrate samples including coumarin hydroxyproducts were excited at 332 nm wavelength by Xe lamp light using luminescence spectrophotometer (Perkin-Elmer 50B). Moreover, the control test of reactive species in phenol decomposition process under UV-vis light irradiation was carried out using different radical scavengers: ammonium oxalate (AO) as scavenger for holes (h^+), silver nitrate (AgNO₃) as scavenger for electrons (e⁻), *p*-benzoquinone (BQ) as scavenger for superoxide radical species (O₂^{·-}) and *tert*-butyl alcohol (t-BuOH) as scavenger for hydroxyl radical species ($\cdot\text{OH}$). The experiment was conducted in similar conditions as phenol degradation under UV-vis light irradiation, expect that small amount of radical scavenger (2 ml) was added to the reaction system.

3. Results and discussion

To investigate the influence of dopant type and amount of rare earth precursor used during hydrothermal synthesis on the physicochemical and photocatalytic properties of RE-K₂Ta₂O₆, a series of samples have been prepared. The description of preparation conditions and properties of as-prepared photocatalysts is shown in Table 1.

3.1. DRS UV-vis spectroscopy

The absorption spectra of pristine K₂Ta₂O₆ and RE-K₂Ta₂O₆ samples in the range of 250–750 nm were converted from DRS UV-vis data by Kubelka-Munk function (K-M function) and the results are presented in Fig. 1. Undoped K₂Ta₂O₆ shows absorption only in UV region. The spectral response of reference sample K₂Ta₂O₆ exhibits absorption edge at about 280 nm followed by a characteristic broad tail between 280 and 350 nm, probably ensuing from mix of pyrochlore and perovskite

Table 1Sample label, preparation conditions and textural properties of $K_2Ta_2O_6$ and RE- $K_2Ta_2O_6$.

Sample label	Rare earth metal dopant (mol%)	BET surface area (m^2/g)	Pore volume (cm^3/g)	Pore diameter (nm)
$K_2Ta_2O_6$	None	2.2	0.0012	2.18
2 mol% Y- $K_2Ta_2O_6$	2.0 Y	8.4	0.0041	1.95
4 mol% Y- $K_2Ta_2O_6$	4.0 Y	7.7	0.0038	1.97
2 mol% Yb- $K_2Ta_2O_6$	2.0 Yb	9.0	0.0046	2.04
4 mol% Yb- $K_2Ta_2O_6$	4.0 Yb	7.6	0.0036	1.89
2 mol% Ho- $K_2Ta_2O_6$	2.0 Ho	7.1	0.0033	1.86
4 mol% Ho- $K_2Ta_2O_6$	4.0 Ho	9.8	0.0050	2.04
2 mol% Pr- $K_2Ta_2O_6$	2.0 Pr	7.7	0.0037	1.92
4 mol% Pr- $K_2Ta_2O_6$	4.0 Pr	6.4	0.0025	1.56
2 mol% Er- $K_2Ta_2O_6$	2.0 Er	10.1	0.0055	2.17
4 mol% Er- $K_2Ta_2O_6$	4.0 Er	9.9	0.0052	2.10
8 mol% Er- $K_2Ta_2O_6$	8.0 Er	7.8	0.0039	2.00
10 mol% Er- $K_2Ta_2O_6$	10.0 Er	6.9	0.0029	1.68

phase [43,44]. It can be clearly seen that, the incorporation of RE ions into $K_2Ta_2O_6$ affects the optical absorption properties of RE- $K_2Ta_2O_6$. The absorption edge of Y, Yb, Ho and Er-doped $K_2Ta_2O_6$ shifts towards shorter wavelength than undoped $K_2Ta_2O_6$. On the other hand, red shift of the absorption edge is observed only in Pr- $K_2Ta_2O_6$ compared to bare $K_2Ta_2O_6$. Stronger absorption towards a longer wavelength can be attributed to enhance charge transfer between RE ion electrons and semiconductor valence band (VB) or conduction band (CB) [45]. Absorption edges of all RE- $K_2Ta_2O_6$ are steep, indicating excitation of electrons from the VB to the CB. The absorption bands in UV-vis region are noticed for Er ion (Fig. 1c), while in only vis region are noticed for Ho ion (Fig. 1b). Erbium dopant has characteristic absorption peaks located at 365, 379, 407, 450, 488, 520, 543 and 653 nm, which can be identified with the transition from the $^4I_{15/2}$ ground state to the excited states of $^4G_{9/2}$, $^4G_{11/2}$, $^2H_{9/2}$, $^4F_{5/2}$, $^4F_{7/2}$, $^2H_{11/2}$, $^4S_{3/2}$ and $^4F_{9/2}$, respectively [46]. The absorption peaks situated at 418, 450, 486 and 642 nm are typical for holmium dopant and can be attributed to transitions from 5I_8 ground state to the excited states of 5G_5 , 5G_6 , 5F_1 , 5F_3 and 5F_5 , respectively [47]. The intensity of Er and Ho absorption peaks increases with increasing their concentration in RE- $K_2Ta_2O_6$. Furthermore, it reveals that probably the majority of RE ions are localized near surface as well as are substituted at K^+ lattice site in $K_2Ta_2O_6$. The mentioned results inform that, the addition of RE dopant into $K_2Ta_2O_6$ semiconductor slightly changes band structure, affecting on their photoabsorbance properties and therefore on photocatalytic activity.

3.2. Nitrogen adsorption measurement

The textural parameters of pristine $K_2Ta_2O_6$ and RE- $K_2Ta_2O_6$ photocatalysts were determined from nitrogen adsorption-desorption measurement and the results are listed in Table 1. All RE-doped $K_2Ta_2O_6$ show higher BET surface area than reference $K_2Ta_2O_6$ ($2.2\text{ m}^2/\text{g}$). The specific surface area of RE- $K_2Ta_2O_6$ fluctuates from 6.4 to $10.1\text{ m}^2/\text{g}$ and is dependent on type and amount of RE dopant in $K_2Ta_2O_6$. The highest BET surface area is observed for 2 mol% Er- $K_2Ta_2O_6$ sample, which is five times higher than primary $K_2Ta_2O_6$. The micro-porosity of RE- $K_2Ta_2O_6$ was examined by measuring pore size distribution, where average pore diameter oscillates in range of 1.56 – 2.17 nm . The smallest value of pore diameter represents 4 mol% Pr- $K_2Ta_2O_6$ sample, while bare $K_2Ta_2O_6$ exhibits pore size of about 2.18 nm . As clearly seen, the surface area increases with increasing corresponding pore diameter in all of RE- $K_2Ta_2O_6$, but pores in RE- $K_2Ta_2O_6$ become smaller than in undoped $K_2Ta_2O_6$. On the other hand, surface area increases with decreasing particle size in almost RE- $K_2Ta_2O_6$ (see in Table 2). It can be explained that, when particle size is decreased, the probability of surface reaction of electrons and holes with water or pollutant molecules is increased, resulting in an increase in photocatalytic performance. Therefore, for RE- $K_2Ta_2O_6$ a decrease in the particle size is more important factor rather than an increase in

surface area, because surface area affects on number of active sites, while particle size influences the distance that photogenerated electrons and holes have to migrate in photocatalyst particle to reach the active sites [27]. Similar results of BET surface area for RE-doped alkali tantalate semiconductors were reported for the 2 mol% La:NaTaO₃ ($4.54\text{ m}^2/\text{g}$) [32], 1 wt% RuO₂/1 wt% La:NaTaO₃ ($13\text{ m}^2/\text{g}$) [31] and La-doped NaTaO₃ ($12.4\text{ m}^2/\text{g}$) [24] prepared by sol-gel method, La:NaTaO₃ ($4.9\text{ m}^2/\text{g}$) [26] synthesized by solid-state reaction and K_{0.9}La_{0.1}TaO₃ ($9.8\text{ m}^2/\text{g}$) [16] obtained by hydrothermal treatment process. Generally, the RE- $K_2Ta_2O_6$ photocatalysts reveal more well-developed specific surface area and narrow pores structure than pure $K_2Ta_2O_6$, which can suppress the recombination of photogenerated electron-hole pairs to achieve higher photocatalytic activity.

3.3. SEM/EDS analysis

The SEM imaging (Fig. 2) and EDS mapping were performed to investigate the effect of RE doping on the morphology of $K_2Ta_2O_6$ material. Fig. 2a and b present the overall SEM view of undoped $K_2Ta_2O_6$, which exhibits regular cube-like shape with smooth surface. Sizes of the cubic particles are generally in the order of few μm (average diameter of about 0.1 – $4.0\text{ }\mu\text{m}$). Some of the smaller microcubes form larger agglomerates. The average edge size of pristine $K_2Ta_2O_6$ microcube is much larger than $K_2Ta_2O_6$ cubic-like crystallite reported by Zhu, et al. ($0.1\text{ }\mu\text{m}$) [13], KTaO₃ octahedra by Zou, et al. ($0.5\text{ }\mu\text{m}$) [48], KTaO₃ nanocube by Wang, et al. (0.2 – $0.25\text{ }\mu\text{m}$) [6] and by Liu, et al. ($0.1\text{ }\mu\text{m}$) [16] prepared in hydrothermal treatment process. The larger size results likely from the addition of the PEG-400 used as a hydrophilic reaction medium during the synthesis. Fig. 2c-f display SEM images of Er-doped $K_2Ta_2O_6$ particles with different dopant

Table 2
Unit cell parameters of $K_2Ta_2O_6$ and RE- $K_2Ta_2O_6$.

Sample label	Lattice parameter a (\AA)		Crystallite size (nm)	
	$K_2Ta_2O_6$	KTaO ₃	$K_2Ta_2O_6$	KTaO ₃
$K_2Ta_2O_6$	10.6140(2)	3.9922(6)	1150	1100
2 mol% Y- $K_2Ta_2O_6$	10.6117(2)	3.9908(7)	550	1700
4 mol% Y- $K_2Ta_2O_6$	10.6121(3)	3.9907(3)	800	600
2 mol% Yb- $K_2Ta_2O_6$	10.6140(2)	3.9922(6)	800	1300
4 mol% Yb- $K_2Ta_2O_6$	10.6099(3)	3.9918(1)	750	4800
2 mol% Ho- $K_2Ta_2O_6$	10.6112(2)	3.9898(3)	550	700
4 mol% Ho- $K_2Ta_2O_6$	10.6088(3)	3.9913(4)	700	550
2 mol% Pr- $K_2Ta_2O_6$	10.6087(2)	3.9899(7)	750	1400
4 mol% Pr- $K_2Ta_2O_6$	10.5915(5)	3.9904(5)	400	1800
2 mol% Er- $K_2Ta_2O_6$	10.6110(1)	3.9892(3)	900	800
4 mol% Er- $K_2Ta_2O_6$	10.6120(3)	3.9899(1)	500	1500
8 mol% Er- $K_2Ta_2O_6$	10.6150(3)	3.9899(4)	750	550
10 mol% Er- $K_2Ta_2O_6$	10.6162(3)	-*	900	-*

*not to calculated

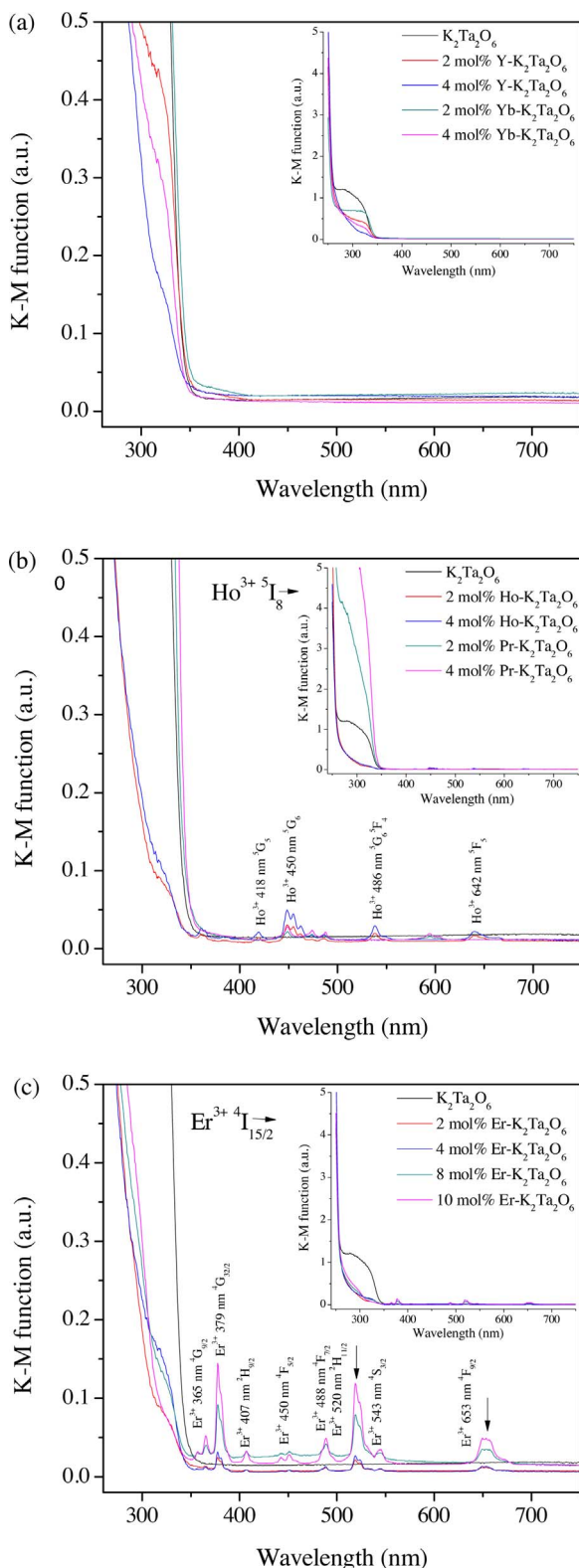


Fig. 1. UV-vis Kubelka-Munk diffuse reflectance absorption of RE-K₂Ta₂O₆ compared to K₂Ta₂O₆ (a) Y-K₂Ta₂O₆ and Yb-K₂Ta₂O₆ (b) Ho-K₂Ta₂O₆ and Pr-K₂Ta₂O₆ (c) Er-K₂Ta₂O₆ with different amount of Er dopant.

concentrations. Introduction of Er ions to the crystal lattice is not significantly affecting the shape and smooth surface of the crystallite. Fig. 3 presents the elemental composition of 2 mol% Er-K₂Ta₂O₆ sample by EDS mapping. It is shown that Er, K, Ta and O elements are indicated and homogeneously distributed in the crystallite. The elemental

concentration of single 2 mol% Er-K₂Ta₂O₆ microcube calculates to 0.74 at% Er-L, 3.26 at% K-K, 14.65 at% Ta-L and 81.35 at% O-K by eZAF quantization method in EDS analysis, which are in good agreement with the results of XPS analysis.

3.4. Powder X-ray diffraction analysis

The powder X-ray diffraction (PXRD) measurement was used to verify the crystalline phase, estimate the lattice parameter, calculate crystallite size and investigate the incorporation of RE ions into the K₂Ta₂O₆ lattice. Fig. 4 shows PXRD patterns of pristine K₂Ta₂O₆ (reference sample), a series of 4 mol% RE-K₂Ta₂O₆ and Er-doped K₂Ta₂O₆ with various dopant concentrations. The diffraction patterns of 2 mol% RE-K₂Ta₂O₆ were also examined (S. 1. – Suppl). The PXRD analysis reveal the presence of potassium tantalate in a form of both pyrochlore (K₂Ta₂O₆) and perovskite (KTaO₃) phases. A symmetry of K₂Ta₂O₆ (*Fd*-3m, space group: 227) is higher than symmetry of KTaO₃ (*Pm*-3m, space group: 221), though the perovskite unit cell is much simpler with more than two times smaller lattice parameter *a*. The PXRD diffraction peaks can be indexed to the (111), (311), (222), (400), (331), (340), (531), (622), (444), (551) and (753) crystallographic planes of K₂Ta₂O₆ (Joint Committee for Power Diffractions Standards, JCPDS cards 35-1464) [43] and to the (100), (110), (111), (200), (210), (211) and (220) crystallographic planes of KTaO₃ (JCPDS cards 77-0918) [13]. For all tested samples, pyrochlore is a majority phase with the highest relative amount of perovskite observed for a reference sample (~8%), 2 mol% Yb-K₂Ta₂O₆ (~11%), 2 mol% Pr-K₂Ta₂O₆ (~11%) and 4 mol% Pr-K₂Ta₂O₆ (~41%) photocatalysts, which is confirmed by the Raman spectroscopy. The highest intensity X-ray diffraction peaks that originate from a perovskite phase are marked by stars (see in Fig. 4). Unit cell parameters of bare K₂Ta₂O₆ and RE-K₂Ta₂O₆ photocatalysts are listed in Table 2. Comparison of the lattice parameter *a* of RE-K₂Ta₂O₆ and pristine K₂Ta₂O₆ is presented in Fig. 5. The LeBail refinement for a reference sample gives lattice constant *a* = 10.6140(2) Å and 3.9922(6) Å for K₂Ta₂O₆ and KTaO₃, respectively. Both values are very close to reported *a* = 10.6189 Å for K_{1.93}Ta₂O_{5.9} [49] and *a* = 3.9883 Å for KTaO₃ [50,51]. Trend lines on Fig. 5a and b represent a slight decrease of the lattice parameter *a* for 2 mol% samples with Y, Ho and Er dopants, for which elements the ionic radius (coordination number N = 6) is r (Y³⁺) = 0.90 Å, r (Ho³⁺) = 0.90 Å and r (Er³⁺) = 0.89 Å [52]. A red lines do not include Pr and Yb ions. The distinctive trend can be explained by lattice contraction effect resulting from a decrease in the ionic radii of tripositive RE ions with increasing atomic number. The reason for the so-called lanthanide contraction refers to imperfect shielding of one 4f electron by another in the same 4f sub-shell. For the series of 4 mol% RE-K₂Ta₂O₆ samples, a similar trend is not observed, which may be due to exceeding the solubility limit of RE ions in K₂Ta₂O₆ (Fig. 5c and d). The average crystallite size of RE-K₂Ta₂O₆, calculated using the Scherrer equation, fluctuates in the range of 400–900 nm and 550–4800 nm for K₂Ta₂O₆ and KTaO₃ phases, respectively (see in Table 2). The particle size of reference K₂Ta₂O₆ is 1150 and 1100 nm for K₂Ta₂O₆ and KTaO₃ phases, respectively. As clearly seen, effect of RE doping causes decrease grain size of RE-K₂Ta₂O₆ crystals for K₂Ta₂O₆ phase. However, this tendency is not observed for RE-K₂Ta₂O₆ particles for KTaO₃ phase, where average crystallite size of 4 mol% Yb-K₂Ta₂O₆ is four times bigger than for reference sample. Theoretically Brus' effective-mass model describes that, band gap of semiconductor particle increases with decreasing its particle size [53]. Therefore smaller particle size of crystal can enhance its photocatalytic activity. The average crystallite size of pristine K₂Ta₂O₆ microcube is much larger than K₂Ta₂O₆ cubic crystallite reported by Zhang, et al. (19 nm) [10] prepared in sol-gel method, K₂Ta₂O₆ and KTaO₃ cubic particles by He, et al. (100 nm and 200 nm, respectively) [8] obtained in solvothermal reaction and KTaO₃ nanocube by Wang, et al. (250 nm) [6] synthesized in hydrothermal treatment process. The larger size results likely from the addition of the PEG-

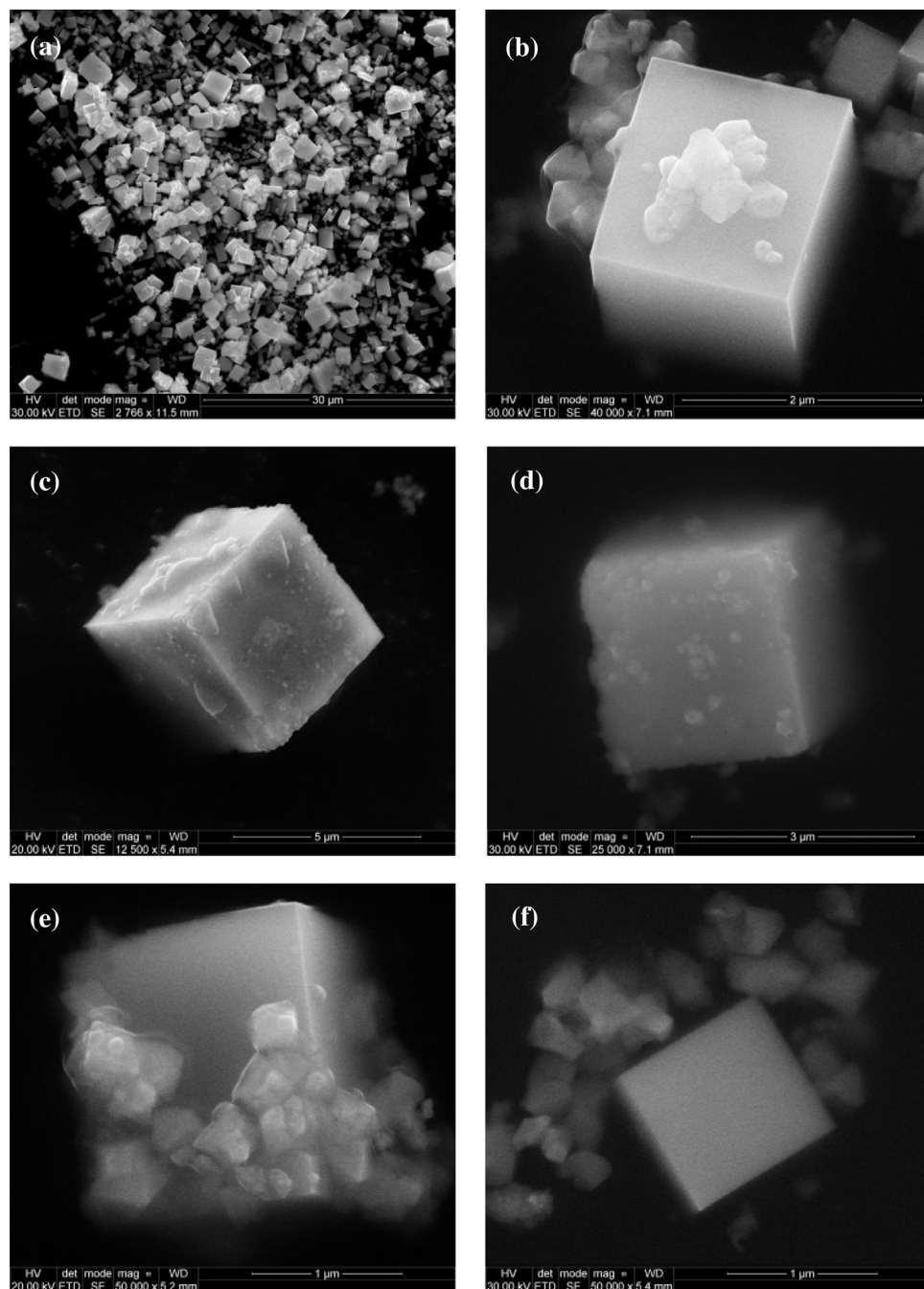


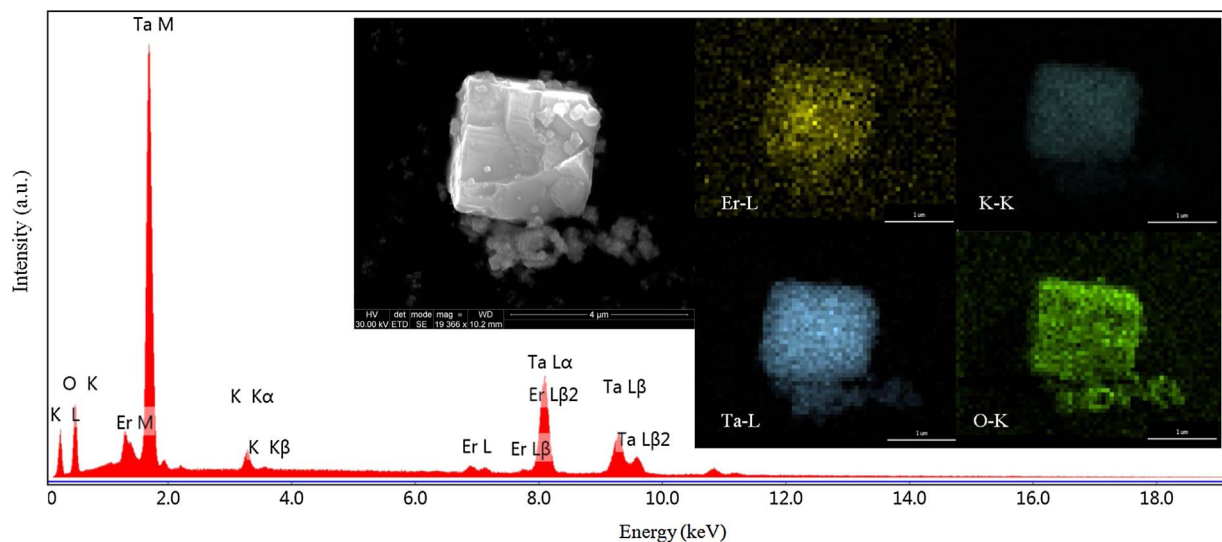
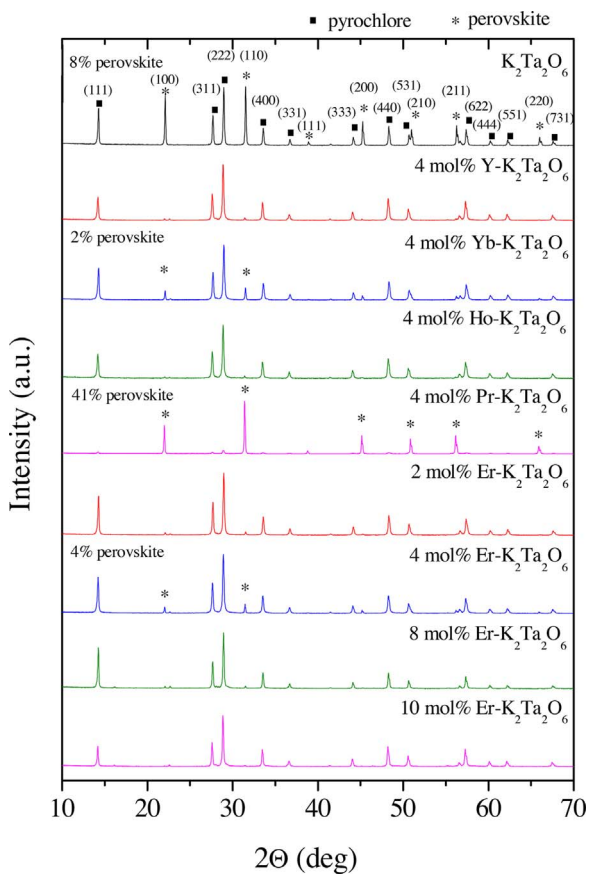
Fig. 2. SEM images of (a, b) $\text{K}_2\text{Ta}_2\text{O}_6$ and (c) 2 mol% Er (d) 4 mol% Er (e) 8 mol% Er and (f) 10 mol% Er dopant in $\text{Er-K}_2\text{Ta}_2\text{O}_6$.

400 used as a hydrophilic reaction medium during the synthesis. Fig. 6a and b present crystal structure of $\text{K}_2\text{Ta}_2\text{O}_6$ and KTaO_3 drawn using VESTA program [54]. In the pyrochlore and the perovskite crystal structure, tantalum ion is located in the center of an octahedron formed by oxygen atoms (TaO_6^{2-}). The ionic radius for pentavalent Ta ion for $N = 6$ is $r(\text{Ta}^{+5}) = 0.64 \text{ \AA}$ [52] and therefore it is unlikely that a rare earth ion $r(\text{RE}^{+3}) \sim 0.9 \text{ \AA}$, $r(\text{Pr}^{4+}) = 0.85 \text{ \AA}$ or $r(\text{Yb}^{2+}) = 1.02 \text{ \AA}$ substitutes this crystallographic site. The other possibility is partial substitution of a potassium site, which ion has a larger ionic radius $r(\text{K}^+) = 1.38 \text{ \AA}$ and 1.64 \AA , for $N = 6$ and 12 , respectively [52,55]. This scenario is supported by two observations: firstly, an estimated lattice parameter a for almost all RE- $\text{K}_2\text{Ta}_2\text{O}_6$ photocatalysts is lower than lattice parameter a for the reference sample; secondly, sub-occupancy of a potassium site was reported by Hu, et al. [49] and Liu, et al. [16]. Summarized, the vacancies at K^+ lattice site in $\text{K}_2\text{Ta}_2\text{O}_6$ can be occupied by RE ions, which confirmed theoretical simulations of the band

structure and partial density of the states (PDOS).

3.5. X-ray photoelectron spectroscopy

Table S1 in supplementary material shows the composition and chemical characters of elements formed in the surface layer of pristine $\text{K}_2\text{Ta}_2\text{O}_6$ and $\text{RE-K}_2\text{Ta}_2\text{O}_6$ photocatalysts with various RE dopant concentration. The presented XPS data were obtained after analysis of high-resolution (HR) XPS spectra of K 2p, C 1s, O 1s, Ta 4d, Er 4d, Ho 4d, Pr 3d Y 4d and Yb 4d for all detected elements potassium, carbon, oxygen, tantalum, erbium, holmium, praseodymium, yttrium and ytterbium, respectively, at the surface area of analyzed samples. The exemplary HR spectra of elements detected on bare $\text{K}_2\text{Ta}_2\text{O}_6$ and on 2 mol% RE- $\text{K}_2\text{Ta}_2\text{O}_6$ are shown in Fig. 7. The fitted spectra of C 1s reveal two carbon peaks at BE of 285 and 286.2 eV, which can be assigned to C–C and C–O groups, respectively [56]. The K 2p line consists of two

Fig. 3. SEM/EDS data and map scanning of 2 mol% Er-K₂Ta₂O₆.Fig. 4. PXRD patterns of K₂Ta₂O₆, 4 mol% RE-K₂Ta₂O₆ and Er-K₂Ta₂O₆ with different amount of Er dopant.

doublets at BE of K 2p_{3/2} at 291.7 and 293.1 eV. The first doublet, with higher intensity peaks, relates to K₂Ta₂O₆ crystal lattice. The second one can be attributed to surface complexes, which can be formed at the surface during preparation of K₂Ta₂O₆. Deconvolution of O 1s spectra reveal four peaks at BE of 529.5, 530.6, 531.7 and 532.8 eV assigned to K₂Ta₂O₆ lattice, surface Me-Ox compounds (Me = Ta, K), -C—O and -OH groups, respectively [56]. Unfortunately, the major Ta 4f spectrum is overlapped by XPS signals originated from RE dopants (Ho 5p_{3/2}, Er 5p_{3/2}, Yb 5p_{3/2}, Y 4p). Thus, the Ta content was evaluated from Ta

4d spectra, which were recorded for both pristine K₂Ta₂O₆ and RE-K₂Ta₂O₆. The bare K₂Ta₂O₆ exhibits the Ta 4d spectrum with Ta 4d_{5/2} signal at BE = 230.0 eV. Detection of HR XPS spectra of RE dopants evidence their successful introduction to the crystal structure as a result of preparation procedure. The Er 4d, Ho 4d, Pr 3d_{5/2}, Y 3d_{5/2} and Yb 4d peak positions located at 169.0, 162.0, 934.0, 157.5 and 185.0 eV, respectively, indicate that RE surface compounds can be attributed to Er₂O₃ [56–59], Ho₂O₃ [56,57,59], Pr₂O₃ [56,57,60,61], Y₂O₃ [56,57,62] and Yb₂O₃ [56–58,63] oxides. The Y 3d spectrum reveals also an additional signal of Y 3d_{5/2} at BE = 159 eV, which can be assigned to hydroxide groups (see in Table S1) or Y-Ox surface species formed as a result of interaction of Y dopant with different crystal phases of K₂Ta₂O₆ and KTaO₃. The various amounts of a perovskite KTaO₃ phase in addition to a major K₂Ta₂O₆ one, were detected by PXRD on all RE-K₂Ta₂O₆ samples. From the other hand, the different interaction between Ta and O in the various KTaO-structures was suggested to be related to the high photocatalytic activity of the K₂Ta₂O₆ sample [64]. In the light of these data, it was interesting to know how RE dopants affect the elemental spectra of primary samples. To elucidate this point, the HR spectra generated by pure K₂Ta₂O₆ were compared to corresponding spectra recorded on Pr-K₂Ta₂O₆ and Er-K₂Ta₂O₆ samples (S. 2. – Suppl and S. 3. – Suppl, respectively). The K 2p spectra recorded on Pr-K₂Ta₂O₆ reveal an additional doublet of narrow peaks at BE of K 2p_{3/2} at 291.6 eV not detected at the primary sample, for both 2 and 4 mol% Pr-K₂Ta₂O₆ samples. That can be interpreted as a result of interaction between growing amount of Pr-dopant with separate K₂Ta₂O₆ and KTaO₃ crystal structures or the new adsorption centers are induced by both coexisting structures. The K 2p spectra collected for Er-K₂Ta₂O₆ became also changed to compare with primary sample. More pronounced rearrangement of the K 2p spectra were observed for samples with nominal Er concentration from 4 to 10 mol %. Deconvoluted O 1s spectrum for the 10 mol% Er-K₂Ta₂O₆ sample disclose larger contribution of hydroxide groups (see in Table S1). The low intensity Er 4d spectra characterize the Er-K₂Ta₂O₆ (see original Er 4d spectra in S. 2. – Suppl). It should be noted that the surface concentration of Er is much lower than predicted by preparation procedure. However, the most distinct discrepancy between Er surface concentrations can be found for 8 and 10 mol% Er-K₂Ta₂O₆ samples. The effect of lanthanide contraction of Er-K₂Ta₂O₆ can be responsible for this phenomenon. This supposition is in line with broadening of the Er 4d spectrum for the 10 mol% Er-K₂Ta₂O₆, which can be induced by mixed states in Er-doped K₂Ta₂O₆ material.

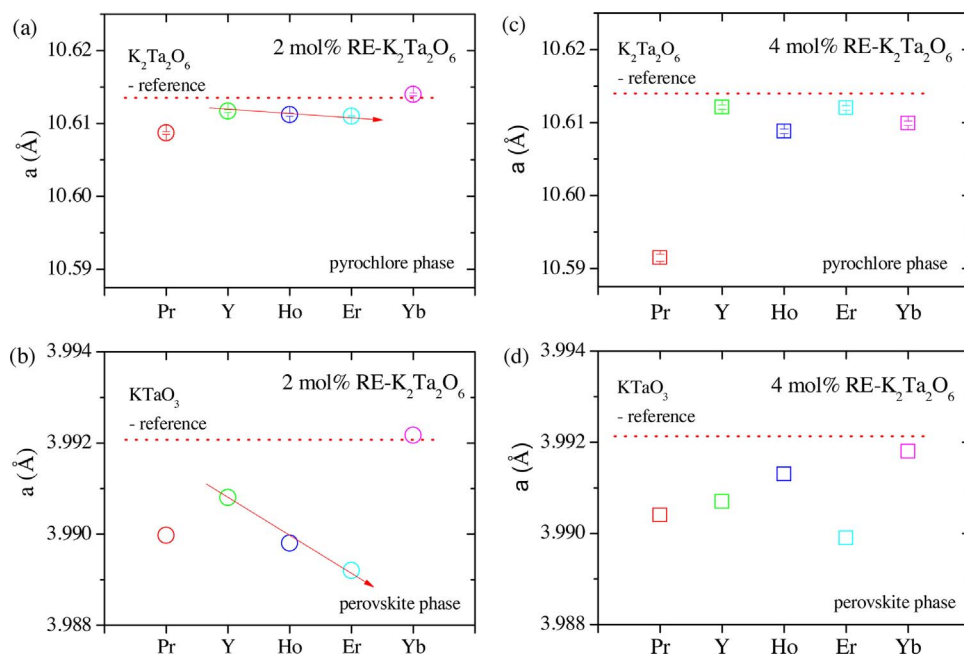


Fig. 5. Comparison of the lattice parameter of pyrochlore and perovskite phases in (a and b) 2 mol% RE-K₂Ta₂O₆ (c and d) 4 mol% RE-K₂Ta₂O₆.

3.6. Raman spectroscopy

The Raman scattering investigation of pristine K₂Ta₂O₆, a series of 4 mol% RE-K₂Ta₂O₆ and Er-doped K₂Ta₂O₆ photocatalysts with various dopant concentrations (Fig. 8) was performed to get additional structural information. It can be clearly seen that, the Raman spectra of Y, Ho and Er-doped K₂Ta₂O₆ are almost similar to scattering pattern of undoped K₂Ta₂O₆. The Raman spectrum of primary K₂Ta₂O₆ does not present well-defined bands in the range of 650–1000 cm⁻¹, instead a broad spectral appears in that region. Further incorporation of Y, Ho and Er ions into K₂Ta₂O₆ primarily causes broadened or shifted the initial Raman bands. Moreover, the intensity of Raman peaks for Er-doped K₂Ta₂O₆ increases with increasing Er dopant from 2 to 10 mol% concentration. Probably, the characteristic phonon frequencies for pyrochlore structure occur at 133, 303, 347, 507 and 646 cm⁻¹. Makarova et al. [65] reported similar characteristic phonon frequencies at 136, 302, 346 and 645 cm⁻¹ for pyrochlore structure in K₂Ta₂O₆ nanocrystal. The phonon frequencies at 507 and 646 cm⁻¹ can be due to contribution Ta–O stretching modes. The Raman bands in region 100–450 cm⁻¹ are assigned to O–Ta–O bending vibrations, while the Raman bands in region 450–900 cm⁻¹ are associated with coupled phonon modes involve the stretching of various Ta–O bonds with different bond strength [29]. On the other hand, the 4 mol% Yb-K₂Ta₂O₆ and 4 mol% Pr-K₂Ta₂O₆ samples show divergent Raman spectra in comparison to the scattering pattern of bare K₂Ta₂O₆. The Raman peak that appears at 135 cm⁻¹ in the 4 mol% Yb-K₂Ta₂O₆ sample is being

markedly more intense. In 4 mol% Pr-K₂Ta₂O₆ sample, Raman peaks positions at 122, 163, 270, 461 and 588 cm⁻¹ exhibit perovskite behavior confirmed by 2TA, LA + TA, TO₂ + TA, 2TO₂, TO₃ + LA and LO₃ + TA phonon modes at 120, 160, 270, 460 and 590 cm⁻¹, respectively [13]. An extra peak position at 216 cm⁻¹ is also observed for the 4 mol% Pr-K₂Ta₂O₆ powder, which may be due to the new surface states in KTaO₃ phase [48]. The differences in the Raman spectra of obtained RE-K₂Ta₂O₆ photocatalysts can be also induced by presence of molecular water, which led to line broadened or shifted [65]. The obtained Raman spectra appear to be in good agreement with results mentioned in XRD analysis.

3.7. Magnetic susceptibility measurement

To investigate the effect of RE doping on K₂Ta₂O₆ magnetic properties, magnetic susceptibility of as-prepared samples were measured. The susceptibility indicates whether a material is attracted into or repelled out of applied magnetic field, which in turn has implications for practical applications, e.g. magnetic separation of photocatalyst particles after process. The mass magnetic susceptibility χ_g for 4 mol% RE-K₂Ta₂O₆ and Er-doped K₂Ta₂O₆ photocatalysts with various dopant concentrations was measured versus temperature T between 2 and 300 K in field of 1 T as shown in Fig. 9. It can be seen that $\chi_g(T)$ for all samples containing RE dopant increases with decreasing temperature. This is a typical behavior for the Curie paramagnetic compounds, that obey the Curie-Weiss law: $\chi_{\text{mol}} = \chi_0 + C/(T-\Theta_{\text{CW}})$, where χ_0 is a

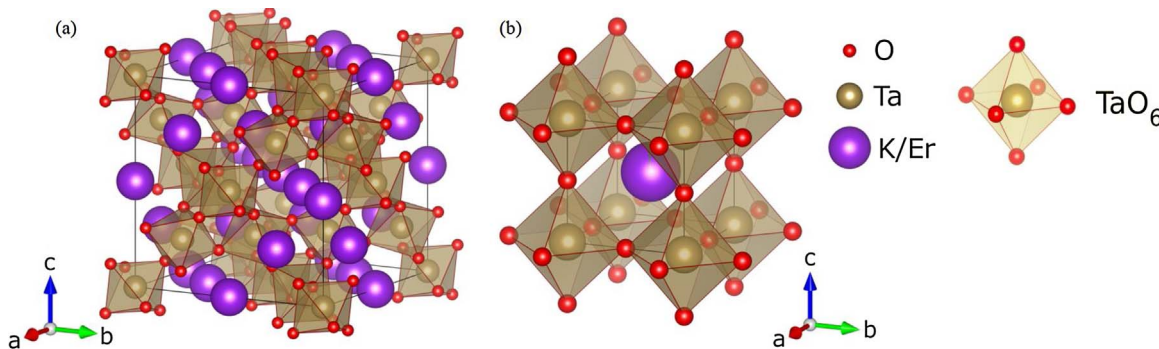


Fig. 6. Visualization of unit cells of (a) pyrochlore and (b) perovskite phases in Er doped potassium tantalate. Image was rendered using VESTA [54].

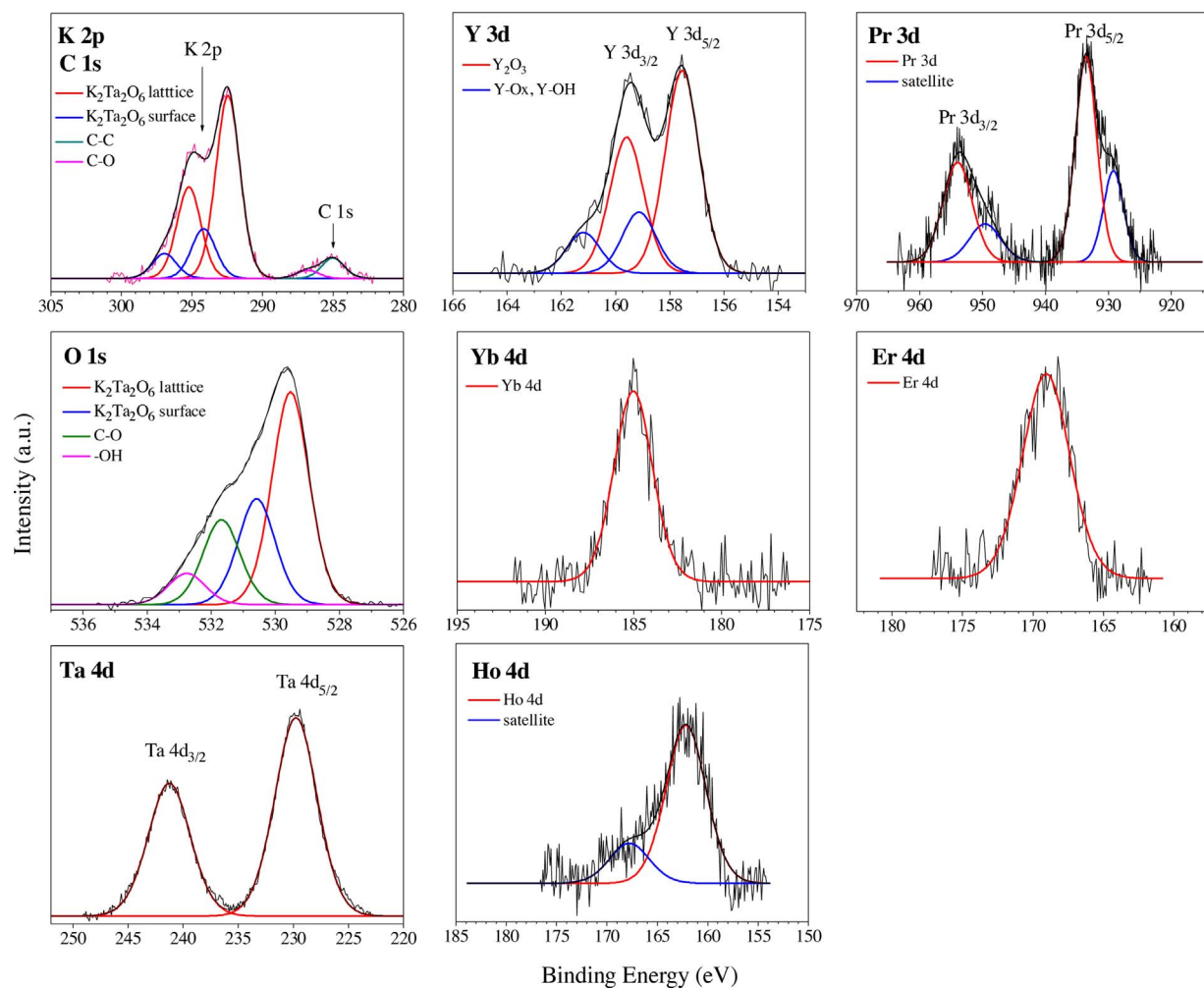


Fig. 7. HR XPS spectra of K 2p, O 1s, Ta 4d, Y 3d, Yb 4d, Ho 4d, Pr 3d, Er 4d measured of K₂Ta₂O₆ and 2 mol% RE-K₂Ta₂O₆.

temperature independent susceptibility, C – Curie constant and Θ_{CW} – Curie-Weiss temperature. The largest and the smallest $\chi_g(2 \text{ K})/\chi_g(300 \text{ K})$ ratio is observed for 4 mol% Ho-K₂Ta₂O₆ and 4 mol% Pr-K₂Ta₂O₆ samples, respectively. This can be explained by the fact that the effective magnetic moment $\mu_{\text{eff}} = 10.4 \mu_B/\text{Ho-mol}$ is the highest and $\mu_{\text{eff}} = 3.5 \mu_B/\text{Pr-mol}$ is the lowest in the used rare earth elements [66]. The effective magnetic moment is related to the Curie constant by $\mu_{\text{eff}} = (3k_B C/N_A)^{1/2}$, where k_B is a Boltzmann constant and N_A is the Avogadro number. The Y dopant does not have a local magnetic moment and therefore χ_g for 4 mol% Y-K₂Ta₂O₆ sample is temperature-independent as can be seen from the inset of Fig. 9a. A negative sign of χ_g indicates that 4 mol% Y-K₂Ta₂O₆ sample is a weakly diamagnetic compound. Temperature dependence of the mass magnetic susceptibility for a series of Er-K₂Ta₂O₆ is presented in Fig. 9b. The higher Er dopant concentration causes increase of the χ_g signal at the same temperature. Since Er is presented at +3 oxidation state and is the only magnetic ion in Er-K₂Ta₂O₆, we can estimate the molar number of Er (n) by assuming $\mu_{\text{eff}} = 9.5 \mu_B/\text{Er-mol}$ and fitting n, χ_0 and Θ_{CW} in the Curie-Weiss law $\chi(T) = (\chi_0 + C/(T-\Theta_{\text{CW}}))/n$. A fit for 10 mol% Er-K₂Ta₂O₆ sample is presented in Fig. 9c. The molar number of Er (n) in a series of Er-K₂Ta₂O₆ increases linearly with increasing nominal concentration of Er. As expected, a trend line (a line in Fig. 9d) for pristine K₂Ta₂O₆ starts from the origin. Summarized, adding a magnetic RE dopant into K₂Ta₂O₆ causes that as-prepared sample obeys the Curie-Weiss law and likely a magnetic separation method can be used after photocatalytic reaction.

3.8. Photoluminescence spectroscopy

Photoluminescence (PL) spectroscopy was used to explore transfer and recombination processes of photogenerated electron-hole pairs in RE-doped K₂Ta₂O₆ photocatalysts. Fig. 10 presents PL spectra of pristine K₂Ta₂O₆ and RE-K₂Ta₂O₆ with excitation at 325 nm wavelength by Xe lamp light. The broadband emission is typical for K₂Ta₂O₆ material [49]. All of RE-K₂Ta₂O₆ samples exhibit maximum emission at around 400–450 nm (blue luminescence) and maximum peak at 525 nm (green luminescence) indicating the complexity of emission mechanism under excitation light. The excitation wavelength from the UV range may induce band to band transition for intrinsic-irradiative emission ($\lambda_{\text{ex}} = 230 \text{ nm}$) or may lead to extrinsic emissions, which are associated with defect states ($\lambda = 270 \text{ nm}$) [49]. Higher energetic photons from the UV range, induce charge transfer between Ta⁵⁺ and O²⁻, and formation of charge transfer states in octahedron complex (TaO₆²⁻). Depending on the Ta–O–Ta bond angle, relaxation of the excitation localized in TaO₆²⁻ may occur to the ground state or may enhance electron-hole pair recombination (as the result of ion vacancies presence and other defects) [67,68]. The first one mechanism leads to the emission with a broadband maximum at around 400–450 nm. In the second one, the energy of the excitation is lowered, and emission occurs at around 525 nm. The most intense emission in PL spectra was recorded for undoped K₂Ta₂O₆. After RE doping into K₂Ta₂O₆, the PL intensity of emission peaks decreases (a trend line in Fig. 10), indicating that the recombination between photoexcited electron-hole pairs is effectively limited by incorporation of RE ions in K₂Ta₂O₆.

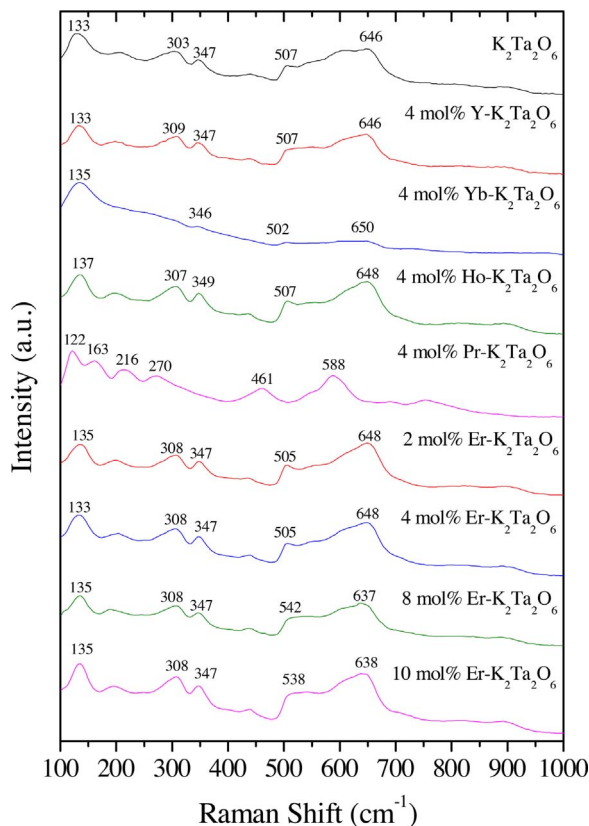


Fig. 8. Raman spectra of $\text{K}_2\text{Ta}_2\text{O}_6$, 4 mol% RE- $\text{K}_2\text{Ta}_2\text{O}_6$ and Er- $\text{K}_2\text{Ta}_2\text{O}_6$ with different amount of Er dopant.

Furthermore, comparing the changes in luminescence intensity of as-prepared Er- $\text{K}_2\text{Ta}_2\text{O}_6$ photocatalysts, it is clearly seen that PL intensity decreases with increasing Er dopant from 2 to 10 mol% concentration. The 8 mol% Pr- $\text{K}_2\text{Ta}_2\text{O}_6$ and 10 mol% Er- $\text{K}_2\text{Ta}_2\text{O}_6$ samples exhibit the lowest luminescence intensity in PL spectra. According to the results, RE doping into $\text{K}_2\text{Ta}_2\text{O}_6$ causes quenching of PL intensity emission due to introduce structural defect and modify charge compensation in the crystal lattice, which clearly confirms that the presence of RE species induces hard suppression of the recombination process of photo-generated electron-hole pairs and therefore can participate in enhanced photocatalytic activity.

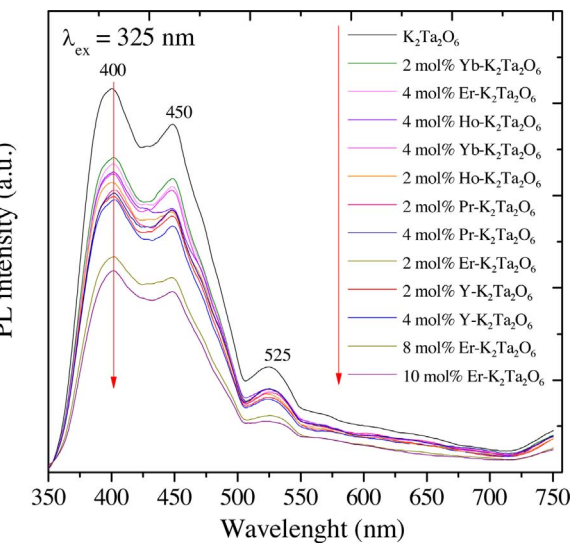


Fig. 10. PL emission spectra of $\text{K}_2\text{Ta}_2\text{O}_6$ and 2 mol% RE- $\text{K}_2\text{Ta}_2\text{O}_6$ excited by Xe lamp light.

3.9. Photocatalytic activity under UV-vis light irradiation

The effect of RE doping on photocatalytic activity of pristine $\text{K}_2\text{Ta}_2\text{O}_6$ and RE- $\text{K}_2\text{Ta}_2\text{O}_6$ materials under UV-vis light irradiation was evaluated in three model reactions by measuring: the decomposition rate of phenol aqueous solution, removal efficiency of gaseous toluene and amount of evolved H_2 in the presence of formic acid solution (Table 3). Moreover, the stability in tree subsequence cycles of the most photoactive samples was investigated for each model reaction.

The phenol photodecomposition rates of pristine $\text{K}_2\text{Ta}_2\text{O}_6$ and RE- $\text{K}_2\text{Ta}_2\text{O}_6$ photocatalysts are listed in Table 3. The kinetics of phenol degradation under UV-vis light irradiation in the presence of as-prepared samples are shown in Fig. 11a. The control test of photolysis exhibits about 8% phenol degradation after 90 min of UV-vis light irradiation, which not significantly affect in the reaction of phenol decomposition with photocatalyst. It can be seen that, all of RE- $\text{K}_2\text{Ta}_2\text{O}_6$ are more photoactive in phenol degradation than pristine $\text{K}_2\text{Ta}_2\text{O}_6$. The efficiency of phenol decomposition after 90 min of UV-vis light irradiation increased from 11 to 33% for undoped $\text{K}_2\text{Ta}_2\text{O}_6$ and 2 mol% Er- $\text{K}_2\text{Ta}_2\text{O}_6$, respectively. The highest photocatalytic activity is observed for 2 mol% Er- $\text{K}_2\text{Ta}_2\text{O}_6$ sample and then decreases for higher concentration (phenol decomposition rate is 1.25, 0.74, 0.88 and

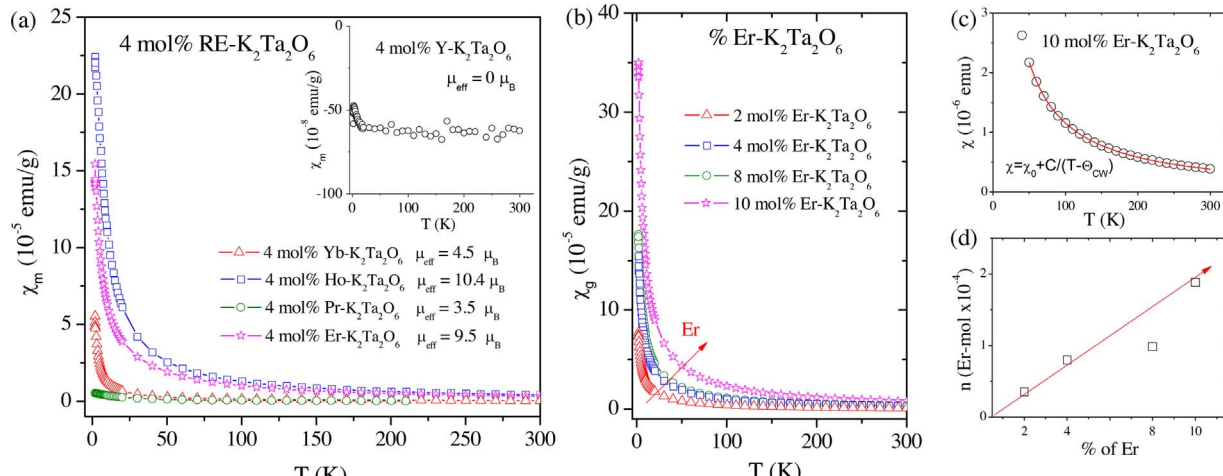


Fig. 9. Magnetic properties: a) mass magnetic susceptibility for 4 mol% RE- $\text{K}_2\text{Ta}_2\text{O}_6$ b) temperature dependence of mass magnetic susceptibility for Er- $\text{K}_2\text{Ta}_2\text{O}_6$ c) fit for 10 mol% Er- $\text{K}_2\text{Ta}_2\text{O}_6$ d) trend line for molar number of Er (n) in Er- $\text{K}_2\text{Ta}_2\text{O}_6$.

Table 3Photocatalyst activity of $K_2Ta_2O_6$ and RE- $K_2Ta_2O_6$.

Sample label	Phenol degradation rate under irradiation after 90 min ($\mu\text{mol}/\text{dm}^3 \text{ min}$)		Toluene removal under UV-vis light irradiation after 60 min (%)		Amount of H_2 under UV-vis light irradiation after 240 min ($\mu\text{mol}/\text{min}$)
	UV-vis light	vis light	1 st cycle	2 nd cycle	
$K_2Ta_2O_6$	0.33	0.06	20	19	7.53
2 mol% Y- $K_2Ta_2O_6$	0.42	0.09	27	21	8.05
4 mol% Y- $K_2Ta_2O_6$	0.48	0.09	29	25	8.62
2 mol% Yb- $K_2Ta_2O_6$	0.58	0.14	36	33	8.86
4 mol% Yb- $K_2Ta_2O_6$	0.52	0.20	30	26	9.73
2 mol% Ho- $K_2Ta_2O_6$	0.50	0.12	21	19	9.18
4 mol% Ho- $K_2Ta_2O_6$	0.51	0.12	22	21	9.08
2 mol% Pr- $K_2Ta_2O_6$	0.83	0.15	45	40	7.58
4 mol% Pr- $K_2Ta_2O_6$	0.81	0.08	40	36	7.99
2 mol% Er- $K_2Ta_2O_6$	1.25	0.23	26	24	9.45
4 mol% Er- $K_2Ta_2O_6$	0.74	0.13	39	35	10.42
8 mol% Er- $K_2Ta_2O_6$	0.88	0.14	36	28	12.51
10 mol% Er- $K_2Ta_2O_6$	0.78	0.13	34	25	15.40

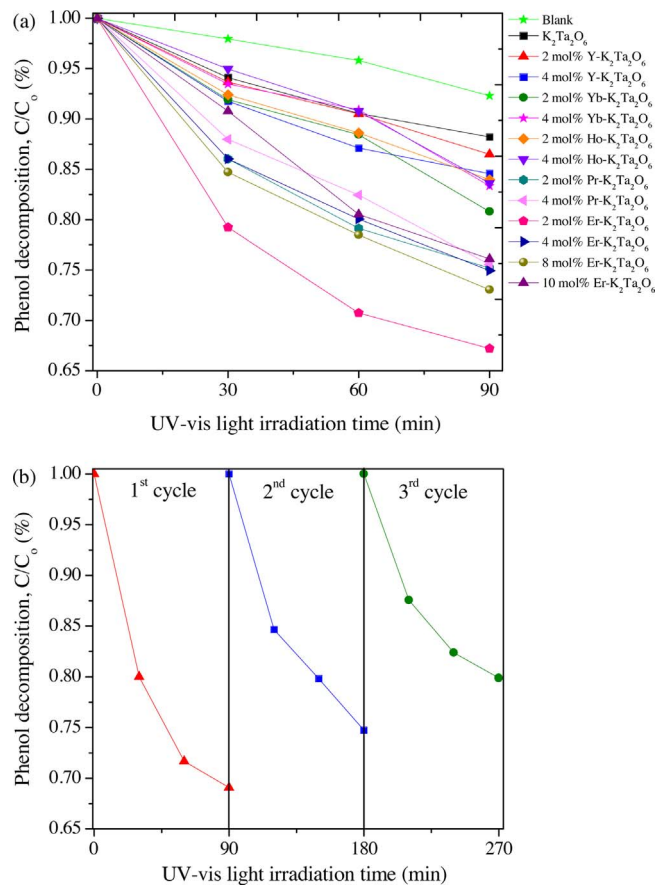


Fig. 11. Phenol decomposition measurement under UV-vis light irradiation a) degradation efficiency of phenol in the presence of $K_2Ta_2O_6$ and RE- $K_2Ta_2O_6$ b) recycling performance of 2 mol% Er- $K_2Ta_2O_6$.

0.78 $\mu\text{mol}/\text{dm}^3 \text{ min}$ for $K_2Ta_2O_6$ doped with 2, 4, 8 and 10 mol% Er, respectively). It may indicate that, optimum content for RE- $K_2Ta_2O_6$ in phenol degradation is 2 mol% RE dopant. Li and Zang also reported the decline in photoactivity of $NaTaO_3:La$ in liquid phase, where too high dose of La dopant in $NaTaO_3:La$ can collapsed active surface sites and thus decreased activity. The highest efficiency of safranine T dye degradation under UV light irradiation was achieved by the sample contained 2 mol% La. Moreover, it was explained that higher photoactivity is attributed to substitution of La^{3+} at Na^+ lattice site, which caused modification in crystal structure and thus delocalization of charge carriers [24]. The lowest photoactivity presents $K_2Ta_2O_6$ doped with 2

and 4 mol% Y (0.42, and 0.48 $\mu\text{mol}/\text{dm}^3 \text{ min}$, respectively). Pristine $K_2Ta_2O_6$ exhibits 0.33 $\mu\text{mol}/\text{dm}^3 \text{ min}$ phenol degradation rate. Moreover, recycling of 2 mol% Er- $K_2Ta_2O_6$ sample was also investigated in phenol decomposition over three subsequence runs (see in Fig. 11b). The photocatalytic activity of 2 mol% Er- $K_2Ta_2O_6$ decreases from 1.10 (1st cycle) to 0.64 $\mu\text{mol}/\text{dm}^3 \text{ min}$ (3rd cycle) phenol degradation rate, which presents beneficial reusability of photocatalyst. The obtained results indicate that, incorporation RE ions into $K_2Ta_2O_6$ lattice enhances its photoactivity in phenol degradation under UV-vis light irradiation.

Additionally, the photocatalytic activity of pristine $K_2Ta_2O_6$ and RE- $K_2Ta_2O_6$ photocatalysts under vis light irradiation was also evaluated by measuring phenol decomposition in aqueous solution. The kinetics of vis-induced phenol degradation in the presence of as-prepared samples are shown in S. 4. – Suppl, while phenol photodecomposition rates of obtained photocatalysts under vis light irradiation are listed in Table 3. It can be seen that, all of RE- $K_2Ta_2O_6$ are more photoactive in phenol decomposition than pristine $K_2Ta_2O_6$, which indicates that RE doping into $K_2Ta_2O_6$ improved its photocatalytic activity under vis light irradiation. However, the efficiency of phenol degradation after 90 min vis light irradiation increased only from 1.8 to 6.7% for undoped $K_2Ta_2O_6$ and 2 mol% Er- $K_2Ta_2O_6$ (as the most photoactive sample), respectively. The obtained results confirmed that, photoactivity of $K_2Ta_2O_6$ is restricted to the UV light region due to its large band gap, in spite of all RE doping into $K_2Ta_2O_6$ slightly improved vis light activity of RE- $K_2Ta_2O_6$.

The efficiency of toluene degradation and stability in two subsequent cycles under UV-vis LEDs light irradiation in the presence of pristine $K_2Ta_2O_6$ and RE- $K_2Ta_2O_6$ photocatalysts are described in Table 3. The kinetics of toluene removal in the first cycle of as-prepared samples are shown in Fig. 12a. The blind test exhibits slightly decreased of toluene concentration in photolysis (about 6%), which not significantly affect in toluene removal process. It can be observed that, the primary $K_2Ta_2O_6$ and RE- $K_2Ta_2O_6$ are photoactive in the toluene degradation. The removal efficiency of bare $K_2Ta_2O_6$ reached about 20% after 60 min of UV-vis LEDs irradiation and remains stable after two subsequent cycles. All of as-prepared samples show higher photocatalytic activity in gas phase than pristine $K_2Ta_2O_6$. The highest photocatalytic activity in toluene degradation after 60 min of UV-vis LEDs light irradiation is observed for 2 mol% Pr- $K_2Ta_2O_6$ and 4 mol% Er- $K_2Ta_2O_6$ samples (45% and 39% in the 1st cycle, respectively). While the lowest toluene removal efficiency is obtained for 2 and 4 mol% Ho-doped $K_2Ta_2O_6$ samples (21% and 22% in the 1st cycle, respectively). It can be correlated with crystal structure, where mix perovskite and pyrochlore-type Pr- $K_2Ta_2O_6$ presents higher toluene removal efficiency than pyrochlore-type Ho- $K_2Ta_2O_6$. Furthermore, the highest

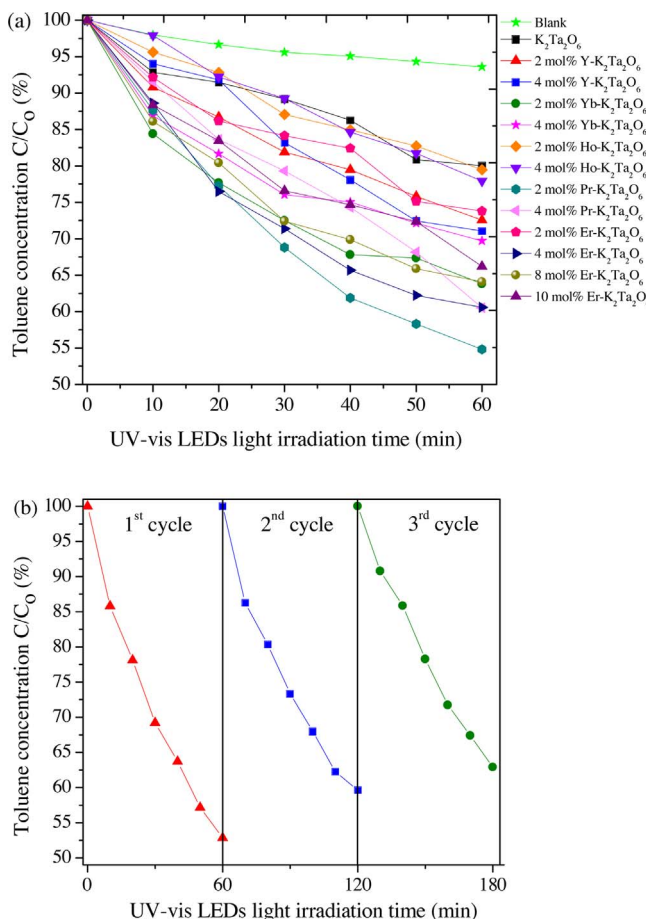


Fig. 12. Toluene degradation process under UV-vis LEDs light irradiation a) removal efficiency of toluene in the presence of K₂Ta₂O₆ and RE-K₂Ta₂O₆ b) recycling performance of 2 mol% Pr-K₂Ta₂O₆.

photocatalytic activity and stability in toluene degradation among Er-K₂Ta₂O₆ samples is obtained for 4 mol% Er dopant (39% in the 1st cycle) and decreased with increasing concentration. Generally, all as-prepared photocatalysts show good photostability in two subsequent cycles in toluene removal under UV-vis LEDs light irradiation. Moreover, photostability of 2 mol% Pr-K₂Ta₂O₆ sample was also checked in toluene degradation over three following runs (see in Fig. 12b). The photocatalytic activity of 2 mol% Pr-K₂Ta₂O₆ decreases from 43% (1st cycle) to 37% (3rd cycle), which shows good lifetime of photocatalyst in practical applications. The lower toluene removal efficiency in next measurement cycles can be result of Pr-K₂Ta₂O₆ surface blocking by adsorbed toluene partial degradation products, as was already observed in modified TiO₂ photocatalysts [69]. Despite this fact, it is shown that RE doping K₂Ta₂O₆ improved its photoactivity in toluene degradation under UV-vis LEDs light irradiation.

First of all, preliminary experiments of H₂ evolution was conducted in different conditions described in S. 5. – Suppl. The obtained results show H₂ production in the presence of undoped K₂Ta₂O₆ from various kinds of organic compounds: methanol, 2-propanol, formic acid, acetic acid and formaldehyde (S. 5a. – Suppl). The largest amount of H₂ is obtained in the presence of formic acid (7.53 μmol/min) compared to acetic acid (1.58 μmol/min), formaldehyde (1.12 μmol/min), 2-propanol (0.86 μmol/min) and methanol (0.34 μmol/min). Moreover, the amount of H₂ increases with increasing concentration of formic acid from 5, 10 and -15% (6.54, 7.53 and 8.56 μmol/min, respectively) (S. 5b – Suppl). It can be explained that, higher concentration of organic compound is more efficient source of electron donors for H₂ evolution [70]. The study of photocatalyst content was examined with the

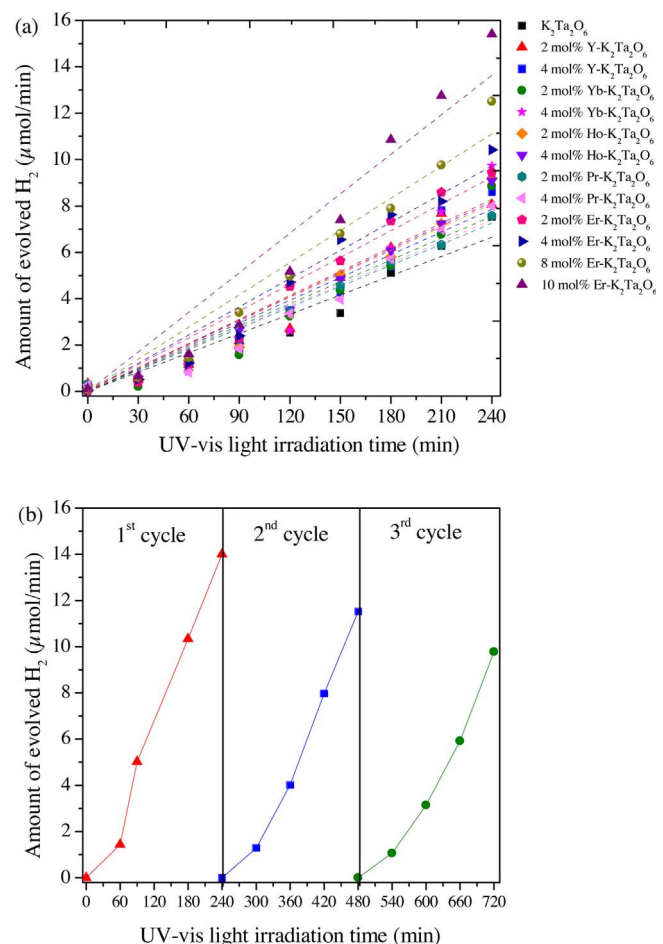


Fig. 13. Photocatalytic H₂ generation under UV-vis light irradiation: a) the amount of evolved H₂ in the presence of K₂Ta₂O₆ and RE-K₂Ta₂O₆ b) recycling performance of 10 mol% Er-K₂Ta₂O₆.

amount of undoped K₂Ta₂O₆ for 0.1, 0.2 and 0.3 g. It can be seen that, optimal content of photocatalyst is 0.2 g (7.53 μmol/min) compared to 0.1 g (5.74 μmol/min) and 0.3 g (6.60 μmol/min) (S. 5c – Suppl). This can be described as shielding effect, which reduces the penetration of light in the solution, occurred after exceeding the optimal content of photocatalyst. The control test was carried out in the presence of formic acid without photocatalyst, where evolution of H₂ is not significant observed (S. 5d – Suppl). Based on these results, the effect of RE doping in K₂Ta₂O₆ was explored in H₂ production. The amount of evolved H₂ in the present of pristine K₂Ta₂O₆ and RE-K₂Ta₂O₆ photocatalysts (0.2 g) from formic acid aqueous solution (C = 10%) are listed in Table 3. The kinetics of H₂ production in the presence of as-prepared samples after 240 min of UV-vis light irradiation are shown in Fig. 13a. It can be seen that, all of RE-K₂Ta₂O₆ exhibit higher activity in H₂ generation from formic acid than pristine K₂Ta₂O₆. The amount of evolved H₂ after 240 min of UV-vis light irradiation is in range of 7.58–15.40 μmol/min for RE-K₂Ta₂O₆ and 7.53 μmol/min for undoped K₂Ta₂O₆. The highest photoactivity is observed for Er-doped K₂Ta₂O₆ samples and increase with increasing concentration (9.45, 10.42, 12.51 and 15.40 μmol/min for 2, 4, 8 and 10 mol% Er-K₂Ta₂O₆, respectively). In opposite, Husin et al. reported that at first photocatalytic H₂ generation over La-doped NaTaO₃ increased with increasing La dopant from 0.5 to 2 mol% (from 0.94 to 1.43 mmol/h, respectively). However, next 5 and 8 mol% La-doped NaTaO₃ samples produced lower amount of evolved H₂ than pristine NaTaO₃ [32]. The lowest photocatalytic activity presents K₂Ta₂O₆ doped with 2 and 4 mol% Pr (7.58 and 7.99 μmol/min, respectively). Furthermore, photostability of 10 mol% Er-K₂Ta₂O₆ sample was also investigated in H₂ evolution from 10%

formic acid over three subsequence runs (see in Fig. 13b). The amount of evolved H₂ decreases from 14.00 μmol/min (1st cycle) to 9.78 μmol/min (3rd cycle), which presents good reusability of photocatalyst.

Summarizing the results of photocatalytic activity, RE doping into K₂Ta₂O₆ lattice enhances its photoactivity under UV-vis light irradiation in pollutant degradation and H₂ generation processes as well as improves photoactivity under vis light irradiation in phenol oxidation. Among selected RE dopant (Y, Yb, Ho, Pr and Er) in K₂Ta₂O₆ structure, the presence of Pr ions is more beneficial for toluene removal, while addition of Er ions is favorable for phenol decomposition and H₂ production. The Pr-doped K₂Ta₂O₆ exhibits the highest photoactivity in gaseous pollutant treatment, which can be attributed to crystallite structure. The incorporation of Y, Yb, Ho and Er ions into K₂Ta₂O₆ caused majority pyrochlore phase formation, while Pr-doped K₂Ta₂O₆ induced mix structure of pyrochlore and perovskite phase. Hence, pyrochlore type Er-doped K₂Ta₂O₆ samples are beneficial in H₂ production. Ishihara et al. reported that, pyrochlore-type crystal showed higher activity for water splitting than perovskite-type photocatalyst. It was explained that octahedron complex (TaO₆²⁻) in K₂Ta₂O₆ is much distorted, therefore charge separation can be easier in K₂Ta₂O₆ than KTaO₃ due to the local polarization effects [11]. Besides, it is revealed that the crystal structure of RE metals containing pyrochlore type mixed oxide is related with ionic radii of RE ions. For instance, RE₂Ti₂O₇ (RE = Eu-Lu, Y) [71] and RE₂Ti₂O₇ (RE = La, Pr, Nd, Sm) [72] samples were obtained as cubic pyrochlore structure and monoclinic perovskite structure, respectively. Moreover, it was demonstrated that, optimal amount of RE dopant in K₂Ta₂O₆ is 2 mol% for phenol decomposition and toluene removal, while content of Er dopant in K₂Ta₂O₆ from 2 to 10 mol%, increase with increasing photoactivity in H₂ generation. The optimal dosage of 2 mol% RE in pollutant degradation may be contributed to the separation of photoinduced electron-hole pairs. Also well-developed specific surface area with narrow pores structure and smaller crystalline size of particles in RE-K₂Ta₂O₆ than K₂Ta₂O₆, can suppress the recombination of photogenerated electron-hole pairs to achieve higher photocatalytic activity. However, photoactivity of as-prepared RE-K₂Ta₂O₆ samples cannot be properly compared in gas and liquid phases because of differ in few aspects: irradiation source and light flux, initial concentration and type of model pollutant or volume of experimental sample used in these measurements.

3.10. PDOS of pristine and RE-doped pyrochlore and perovskite structure

Systematic theoretical simulations were performed to investigate the localization of RE ions in K₂Ta₂O₆ and KTaO₃ structure. The electronic structure and partial density of the states (PDOS) of RE-doped K₂Ta₂O₆ and RE-doped KTaO₃ systems were investigated and then compared to bulk structure of K₂Ta₂O₆ and KTaO₃. Fig. 14 displays PDOS of both pristine pyrochlore-type K₂Ta₂O₆ (Fig. 14a) and

perovskite-type KTaO₃ (Fig. 14b) structures. In both systems, the electronic structure of the upper part of the valence band (VB) has mainly O 3p character, while the main contribution in the lower part of the conduction band (CB) comes from Ta 5d states. Fig. 15a and b presents the atomic structure for doped pyrochlore-type Er/Pr-K₂Ta₂O₆ and perovskite-type Er/Pr-KTaO₃. Computed PDOS for Er-K₂Ta₂O₆, Er-KTaO₃, Pr-K₂Ta₂O₆ and Pr-KTaO₃ systems (Fig. 15c-f) show that in all cases, a formation of a shallow defective level within the band gap close to the band edge of the CB. For the case of Er-doped K₂Ta₂O₆/KTaO₃, the defective level is formed by Er 4f states. The energy difference between the Er 4f states at the Fermi level and the lowest peak of the unoccupied Ta 5d states for Er-K₂Ta₂O₆ and Er-KTaO₃ are 1.3 eV and 0.62 eV, respectively (cf. Fig. 15c and d). For the case of Pr-K₂Ta₂O₆, the defective level is formed by Pr 4d + 4f states with considerable contribution of K 4p + 4s states at the Fermi level; the energy difference between Fermi energy and the unoccupied peak, that is composed by Ta 6s + 5d, states is 0.51 eV (cf. Fig. 15e). The system Pr-KTaO₃ shows a shallow defective level composed mainly of Pr 4f states at the Fermi level and the energy difference to the closest unoccupied peak, that is composed by Pr 4f and Ta 5d, is 0.3 eV (cf. Fig. 15f). In summary, the incorporation of RE (i.e. Pr, Er) ions at K⁺ lattice site in RE-doped K₂Ta₂O₆/KTaO₃ structure lead, in most of the cases, to the formation of RE 4f states below the conduction band of K₂Ta₂O₆/KTaO₃ in electronic structure, except for Pr-K₂Ta₂O₆, where density functional theory (DFT) calculations suggest that defective level is composed by a mixture of Pr 4d + 4f with K 4p + 4s states.

3.11. Discussion of photocatalytic mechanism

The results of photocatalytic experiments show degradation of pollutants and H₂ generation in the presence of RE-K₂Ta₂O₆ under UV-vis light irradiation. To understand the photocatalytic mechanism of as-prepared samples, the formation of hydroxyl radicals (·OH) under UV-vis light irradiation were detected by fluorescence (FL) technique using coumarin as trapping agent. The evaluated ·OH radicals reacted with coumarin to produce fluorescent 7-hydroxycoumarin, which was measured at around 456 nm wavelength. It was revealed nearly linear relationship between fluorescent intensity of product and irradiation time. Fig. 16 presents efficiency of ·OH radicals generation on the surface of pristine K₂Ta₂O₆ and 2 mol% RE-K₂Ta₂O₆ photocatalysts under UV-vis light irradiation. The control test of ·OH radicals production confirmed that FL peak was not observed under UV-vis light irradiation in the absence of photocatalysts, which suggests that fluorescence product is generated by chemical reaction in the present of K₂Ta₂O₆ and RE-K₂Ta₂O₆. Among 2 mol% RE-K₂Ta₂O₆ samples, incorporation of 2 mol% Er dopant into K₂Ta₂O₆ leads to formation the highest amount of evaluated ·OH radicals in comparison to undoped K₂Ta₂O₆, therefore indicates the highest photocatalytic activity. The

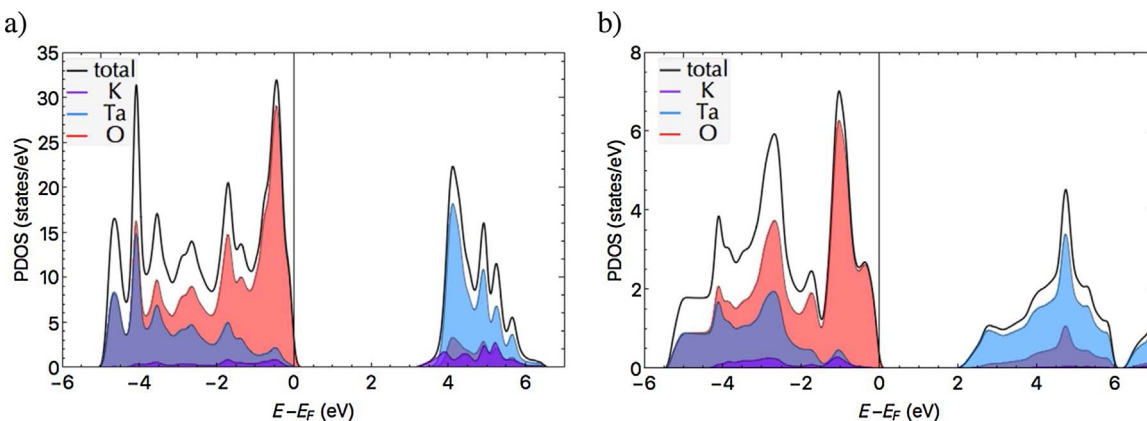


Fig. 14. Computed PDOS for bulk structure of a) K₂Ta₂O₆ and b) KTaO₃. The vertical dash line represents the Fermi level.

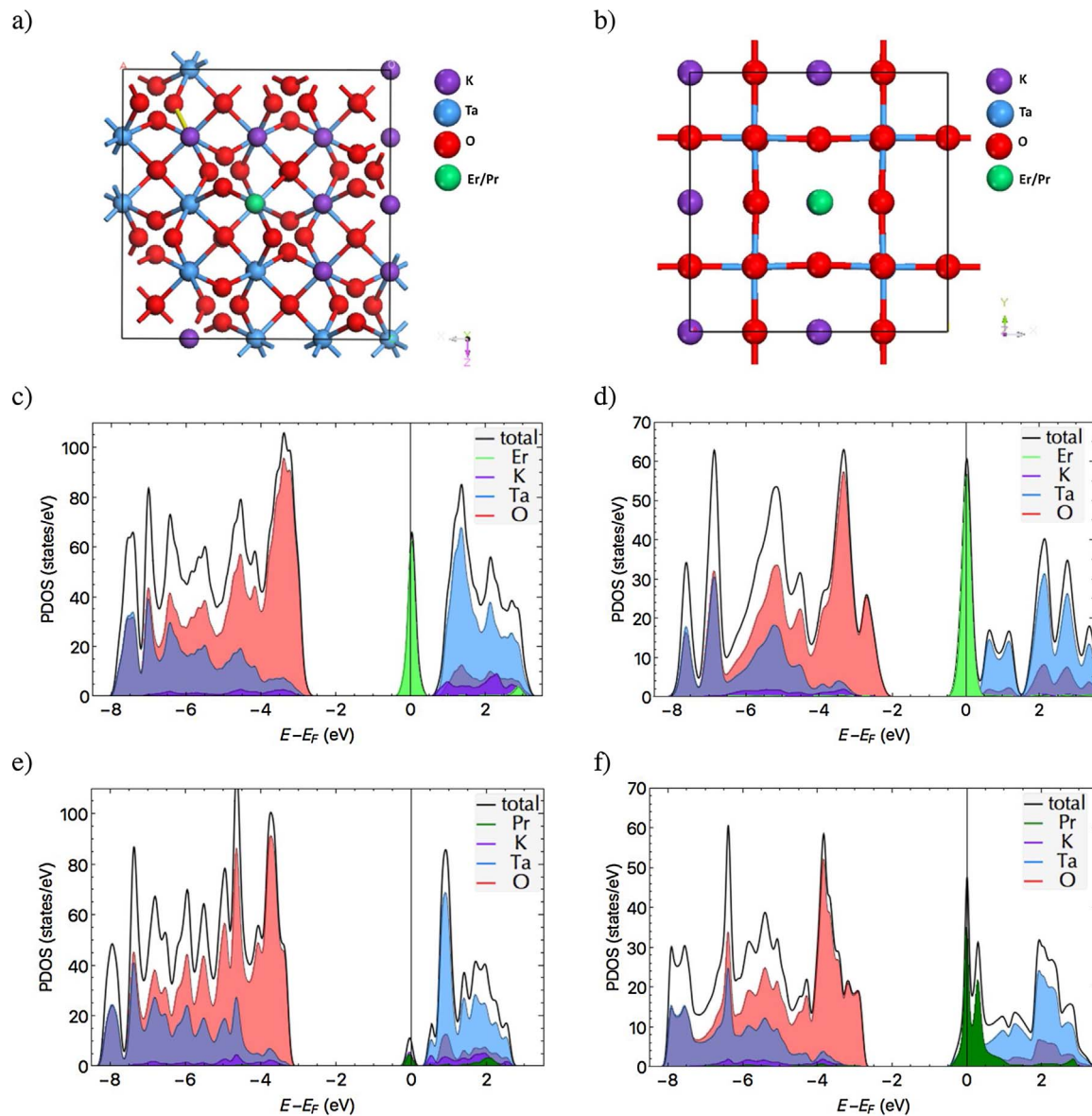


Fig 15. The atomic and electronic structure for doped (a) pyrochlore-type Er/Pr-K₂Ta₂O₆ and (b) perovskite-type Er/Pr-KTaO₃; computed PDOS for (c) Er-K₂Ta₂O₆ (d) Er-KTaO₃ (e) Pr-K₂Ta₂O₆ (f) Pr-KTaO₃.

obtained results are in good agreement with photocatalytic activity in phenol decomposition. Moreover, the control test of reactive species in phenol degradation process was carried out using different radical scavengers: ammonium oxalate (AO) as scavenger for holes (h^+), silver nitrate ($AgNO_3$) as scavenger for electrons (e^-), *p*-benzoquinone (BQ) as scavenger for superoxide radical species ($O_2\cdot^-$) and *tert*-butyl alcohol (t-BuOH) as scavenger for hydroxyl radical species ($\cdot OH$). The measurement was conducted for 2 mol% Er-K₂Ta₂O₆ sample, which exhibits the highest photocatalytic activity in the phenol oxidation under UV-vis light irradiation (Fig. 17). It can be seen that, addition of t-BuOH and BQ greatly inhibited phenol decomposition, which means that evolved $\cdot OH$ and $O_2\cdot^-$ radicals are the main active species in degradation process. The introduction of AO suppresses the phenol oxidation causing around 20% lower degradation efficiency, while in the present of $AgNO_3$ photocatalytic activity decrease about 15% than for sample with no scavenger. Obtained results show that, except e^- , photogenerated h^+ , evolved $\cdot OH$ and $O_2\cdot^-$ radicals are actively involved in phenol degradation under UV-vis light irradiation. For instance, Xu et al. reported that decomposition behavior of tetracycline under vis light irradiation in the presence of 3 mol% Ag-K₂Ta₂O₆ was

inhibited by 2-propanol ($\cdot OH$ scavenger) and increased in the presence of $AgNO_3$ (e^- scavenger). It was suggested that $AgNO_3$ had less opportunity in recombination of photogenerated electron-hole pairs and facilitated production more holes [43].

Based on above results, a possible mechanism for the photocatalytic processes of RE-K₂Ta₂O₆ under UV-vis light irradiation is proposed in Fig. 18. Probably, incorporation of Y, Yb, Ho, Pr and Er ions at K⁺ lattice site in K₂Ta₂O₆, contributes to formation monotonically lower position of new RE 4f levels in the electronic structure across RE ions with increasing the number of 4f electrons. The RE 4f states are situated below CB edge within the band gap, which confirmed computer simulations of band structure and PDOS. The unoccupied and occupied RE 4f orbitals are not completely localized but partially contribute to the hybridization with O 2p and Ta 5d orbitals. Hence, the photocatalytic activity is likely related to the degree of RE-O-Ta hybridization, which affects on band structure and is also dependent on the chemical composition and crystal formation [35]. Tantalate oxide exhibits negative CB edge potential vs. $O_2/O_2\cdot^-$ reduction level and possesses delocalized nature of photoexcited electron-hole pairs. In photocatalytic H₂ generation the position of CB is the dominant factor in evolved H₂

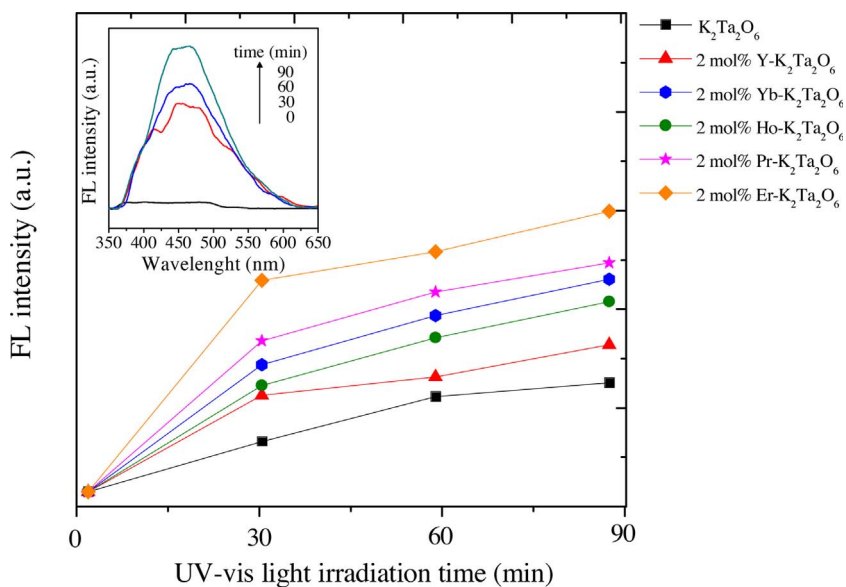


Fig 16. Efficiency of ·OH generation on the surface of K₂Ta₂O₆ and 2 mol% RE-K₂Ta₂O₆ under UV-vis light irradiation. Insert graph presents FL spectrum of 2 mol% Er-K₂Ta₂O₆.

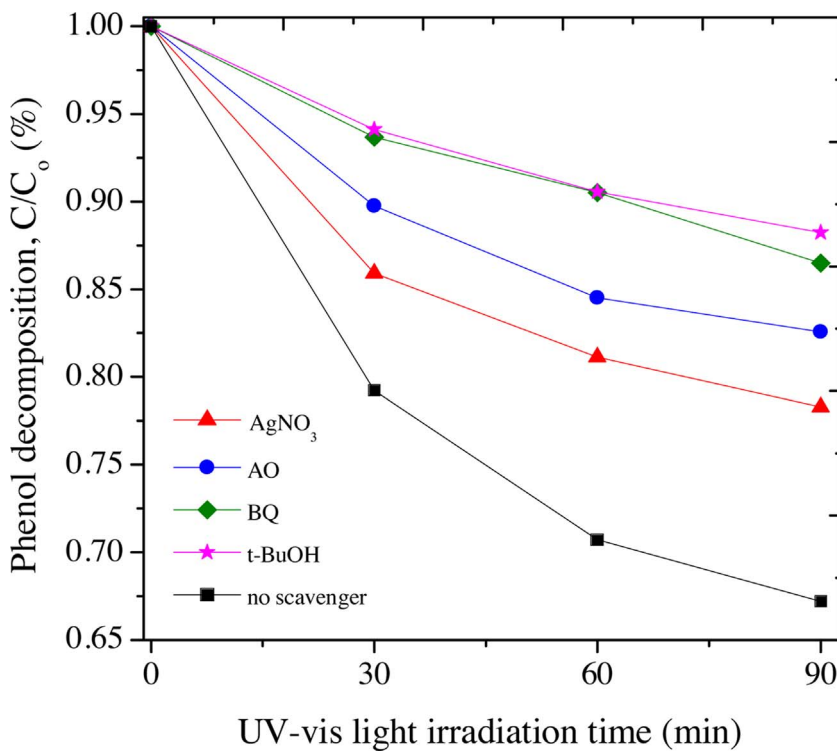


Fig 17. Effect of different scavengers in phenol degradation under UV-vis light irradiation in the presence of 2 mol% Er-K₂Ta₂O₆.

generation, while the position of VB has the major impact in formation ·OH radicals in organic compound degradation [73]. Fig. 18a presents the mechanism of pollutant decomposition over photocatalyst under UV-vis light irradiation, which involves the photoexcited charges (electron-hole pairs). The electrons from CB react with dissolved O₂ in water on the photocatalyst surface to generate O₂^{·-} radicals, while the holes in VB absorbed H₂O on the surface of photocatalyst to produce ·OH radicals. These active oxygen species can cause mineralization and oxidize pollution into CO₂ and H₂O [73]. On the other hand, mechanism of H₂ generation (Fig. 18b) can be explained that the molecules of water in the formic acid solution react with holes in VB causing split into ·OH radicals and H⁺ ions (H₂O oxidation). The obtained ·OH radicals generate O₂, while excited electrons from CB are withdrawn by hole ions, resulting in evolution of H₂. Addition of organic compound as scavenger agent (i.e. HCOOH) is efficient source of electron donors for

H₂ evolution [70]. It is also noticed that photogenerated electrons in CB can recombine with photogenerated holes in VB to dissipate the input energy in form of radiated light or heat [74].

4. Conclusions

Concluding, for the first time, this study presents complete physicochemical characterization and theoretical calculation of K₂Ta₂O₆ doped with rare earth ions (Y, Yb, Ho, Pr, Er) to deduce the photocatalytic reactivity in organic degradation treatments (phenol in liquid phase and toluene in gas phase) and H₂ generation process. It is found out that, trivalent RE ion is likely partial substituted at K⁺ lattice site in RE-K₂Ta₂O₆ structure. The incorporation of Y, Yb, Ho and Er ions into K₂Ta₂O₆ caused majority pyrochlore phase formation and therefore improved photocatalytic activity in H₂ production, while Pr-doped

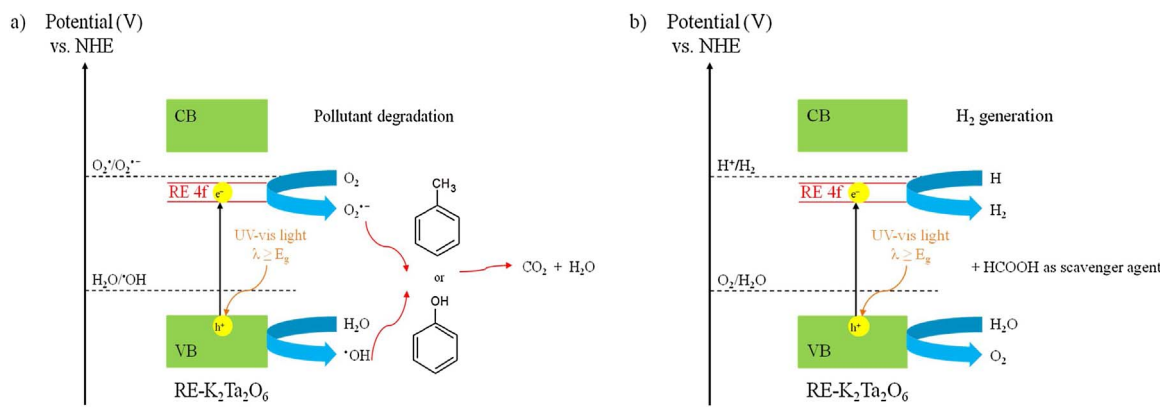


Fig. 18. Proposed mechanism of photocatalytic processes a) pollutant degradation and b) H_2 generation under UV-vis light irradiation in the presence of $\text{RE-K}_2\text{Ta}_2\text{O}_6$.

$\text{K}_2\text{Ta}_2\text{O}_6$ induced mix structure of pyrochlore and perovskite phase, which enhanced photoactivity in gaseous pollutant treatment. Moreover, incorporation of Er or Pr ions into $\text{K}_2\text{Ta}_2\text{O}_6$ is beneficial for aqueous pollutant purification. The highest photocatalytic performance under UV-vis light irradiation is observed for 2 mol% $\text{Er-K}_2\text{Ta}_2\text{O}_6$ (33% of phenol decomposition), 2 mol% $\text{Pr-K}_2\text{Ta}_2\text{O}_6$ (45% of toluene removal) and 10 mol% $\text{Er-K}_2\text{Ta}_2\text{O}_6$ (15.40 $\mu\text{mol}/\text{min}$ of evolved H_2 from 10% formic acid), respectively. Surface morphology of as-prepared Er-doped $\text{K}_2\text{Ta}_2\text{O}_6$ samples exhibits regular cube-like shape particles with well-developed specific surface area. The PL spectra expose that, RE dopant induces hard suppression of the recombination of photo-generated electron-hole pairs compared to undoped $\text{K}_2\text{Ta}_2\text{O}_6$. The radical capture experiments confirm that $\cdot\text{OH}$ and $\text{O}_2^{\cdot-}$ radicals are the main active species in phenol degradation process. Based both on experimental work and computer simulations of band structure and PDOS, it is proposed that during the hydrothermal synthesis, new RE 4f states below the CB of $\text{RE-K}_2\text{Ta}_2\text{O}_6$ are formed, which may reduce the photoexcitation energy from the VB to the CB under UV-vis light irradiation. Summarized, the improvement in photoactivity of $\text{RE-K}_2\text{Ta}_2\text{O}_6$ materials can be achieved by specific physicochemical properties due to incorporation of RE ions into $\text{K}_2\text{Ta}_2\text{O}_6$. The $\text{RE-K}_2\text{Ta}_2\text{O}_6$ photocatalysts are promising materials in photocatalytic purification pollutants and in environmental green energy production. This work may provide valuable information for RE doping semiconductor photocatalysts with enhanced UV-vis photocatalytic performance.

Acknowledgement

This research was financially supported by University of Gdansk (PROJECT BMN nr 538-8625-B050-15).

Appendix A. Supplementary data

Supplementary data associated with this article can be found, in the online version, at <http://dx.doi.org/10.1016/j.apcatb.2017.10.061>.

References

- [1] T. Kamegawa, Y. Shimizu, H. Yamashita, *Adv. Mater.* 24 (2012) 3697–3700.
- [2] C. Sarantopoulos, E. Puzenat, C. Guillard, J.-M. Herrmann, A.N. Gleizes, F. Maury, *Appl. Catal. B* 91 (2009) 225–233.
- [3] D. Venieri, A. Fragedaki, M. Kostadima, E. Chatzisymeon, V. Binas, A. Zachopoulos, G. Kiriakidis, D. Mantzavinos, *Appl. Catal. B* 154–155 (2014) 93–101.
- [4] A.L.A. Marinho, R.C. Rabelo-Neto, F.B. Noronha, L.V. Mattos, *Appl. Catal. B* 520 (2016) 53–64.
- [5] S. Zlotnik, S.K. Sahu, A. Navrotsky, P.M. Vilarinho, *Chem. Eur. J.* 21 (2015) 1–8.
- [6] X. Wang, S. Zheng, Y. Zhang, *Mater. Lett.* 62 (2008) 1212–1214.
- [7] W.-P. Tai, *Mater. Sci. Eng. B* 103 (2003) 83–87.
- [8] Y. He, Y. Zhu, N. Wu, *J. Solid State Chem.* 177 (2004) 2985–2990.
- [9] J.W. Liu, G. Chen, Z.H. Li, Z.G. Zhang, *Int. J. Hydrogen Energy* 32 (2007) 2269–2272.
- [10] G. Zhang, W. Jiang, S. Yu, *Mater. Res. Bull.* 45 (2010) 1741–1747.
- [11] T. Ishihara, N. Baik, N. Ono, H. Nishiguchi, Y. Takita, *J. Photochem. Photobiol. A* 167 (2004) 149–157.
- [12] J. Wang, C. Xiao, X. Wu, G. Zhang, *Chin. J. Chem.* 35 (2017) 189–195.
- [13] S. Zhu, H. Fu, S. Zhang, L. Zhang, Y. Zhu, *J. Photochem. Photobiol. A: Chem.* 193 (2008) 33–41.
- [14] I.E. Paulauskas, J.E. Katz, G.E. Jellison Jr., N.S. Lewis, L.A. Boatner, G.M. Brown, *J. Electrochem. Soc.* 156 (2009) B580–B587.
- [15] F. Rossella, L. Peruccini, P. Galinetto, G. Samoggia, M.C. Mozzati, C.B. Azzoni, A.G. Badalyan, V.A. Trepakov, P.P. Syrnikov, *Phys. Stat. Sol. 4* (2007) 1101–1104.
- [16] X. Liu, J. Lv, S. Wang, X. Li, J. Lang, Y. Su, Z. Chai, X. Wang, *J. Alloy Compd.* 622 (622) (2015) 894–901.
- [17] T. Ishihara, H. Nishiguchi, K. Fukamachi, Y. Takita, *J. Phys. Chem. B* 103 (1999) 1–3.
- [18] H. Gan, G. Zhang, H. Huang, *J. Hazard Mater.* 250–251 (2013) 131–137.
- [19] A.R. Benrekia, N. Benkhetou, A. Nassour, M. Driz, M. Sahnoun, S. Lebegue, *Physica B* 407 (2012) 2632–2636.
- [20] T.P. Sinha, A. Dutta, S. Saha, K. Tarafder, B. Sanyal, O. Eriksson, A. Mookerjee, *Physica B* 407 (2012) 4615–4621.
- [21] B. Modak, S.K. Ghosh, *Sol. Energy Mater. Sol. C* 159 (2017) 590–598.
- [22] V. Jeyalakshmi, R. Mahalakshmy, K.R. Krishnamurthy, B. Viswanathan, *Catal. Today* 266 (2016) 160–167.
- [23] V. Jeyalakshmi, S. Tamilmani, R. Mahalakshmy, P. Bhyrappa, K.R. Krishnamurthy, B. Viswanathan, *J. Mol. Catal. A* 420 (2016) 200–207.
- [24] X. Li, J. Zang, *Catal. Commun.* 12 (2011) 1380–1383.
- [25] L.M. Torres-Martinez, A. Cruz-Lopez, I. Juarez-Ramirez, M.E. Meza-de la Rosa, *J. Hazard. Mater.* 165 (2009) 774–779.
- [26] Z. Wu, G. Li, F. Zhang, W. Zhang, *Appl. Surf. Sci.* 319 (2014) 372–375.
- [27] A. Kudo, H. Kato, *Chem. Phys. Lett.* 331 (2000) 373–377.
- [28] Y. Li, S. Li, Y. Guo, J. Wang, *Int. J. H2 Energy* 39 (2014) 17608–17616.
- [29] P. Jana, C.M. Montero, P. Pizarro, J.M. Coronado, D.P. Serrano, V.A. de la Pena O'Shea, *Int. J. Hydrogen Energy* 39 (2014) 5283–5290.
- [30] A. Iwase, H. Kato, A. Kudo, *Appl. Catal. B* 136 (2013) 89–93.
- [31] L.M. Torres-Martinez, R. Gomez, O. Vazquez-Cuchillo, I. Juarez-Ramirez, A. Curoz-Lopez, F.J. Alejandro-Sandoval, *Catal. Commun.* 12 (2010) 268–272.
- [32] H. Husin, H.-M. Chen, W.-N. Su, C.-J. Pan, W.-T. Chuang, H.-S. Sheu, B.-J. Hwang, *Appl. Catal. B* 102 (2011) 343–351.
- [33] H. Husin, W.-N. Su, H.-M. Chen, C.-J. Pan, S.-H. Chang, J. Rick, W.-T. Chuang, H.-S. Sheu, B.-J. Hwang, *Green. Chem.* 13 (2011) 1745–1754.
- [34] X. Fu, X. Wang, D.Y.C. Leung, W. Xue, Z. Ding, *Catal. Commun.* 12 (2010) 184–187.
- [35] M. Machida, S. Murakami, T. Kijima, S. Matsushima, M. Arai, *J. Phys. Chem. B* 105 (2001) 3289–3294.
- [36] G. Kresse, J. Hafner, *Phys. Rev. B* 47 (1993) 558–561.
- [37] G. Kresse, J. Hafner, *Phys. Rev. B* 49 (1994) 14251–14269.
- [38] G. Kresse, J. Furthmuller, *Comput. Mater. Sci.* 6 (1996) 15–50.
- [39] J.P. Perdew, J.A. Chevary, S.H. Vosko, K.A. Jackson, M.R. Pederson, D.J. Singh, C. Fiolhais, *Phys. Rev. B: Condens. Matter Mater. Phys.* 46 (1992) 6671–6687.
- [40] P.E. Blöchl, *Phys. Rev. B* 50 (1994) 17953–17979.
- [41] G. Kresse, D. Joubert, *Phys. Rev. B* 59 (1999) 1758–1775.
- [42] J.P. Perdew, K. Burke, M. Ernzerhof, *Phys. Rev. Lett.* 77 (1996) 3865–3868.
- [43] D. Xu, K. Liu, W. Shi, M. Chen, B. Luo, L. Xiao, W. Gu, *Ceram. Int.* 41 (2014) 4444–4451.
- [44] D. Xu, S. Yang, Y. Jiu, M. Chen, W. Fan, B. Luo, W. Shi, *Langmuir* 31 (2015) 9694–9699.
- [45] A.-W. Xu, Y. Gao, H.-Q. Liu, *J. Catal.* 207 (2002) 151–157.
- [46] Y. Yang, C. Zhang, Y. Xu, H. Wang, X. Li, C. Wang, *Mater. Lett.* 64 (2010) 147–150.
- [47] B. Karmakar, *J. Solid State Chem.* 178 (2005) 2663–2672.
- [48] Y. Zou, Y. Hu, H. Gu, Y. Wang, *Mater. Chem. Phys.* 115 (2009) 151–153.
- [49] C.-C. Hu, T.-F. Yeh, H. Teng, *Catal. Sci. Technol.* 3 (2013) 1798–1804.
- [50] A. Tkach, P.M. Vilarinho, A. Almeida, *J. Eur. Ceram. Soc.* 31 (2001) 2303–2308.
- [51] E.A. Zhurova, Y. Ivanov, V. Zavodnik, V. Tsirelson, *Acta Cryst. B* 56 (2000) 594–600.
- [52] R.D. Shannon, *Acta Cryst. A* 32 (1976) 751–767.
- [53] H. Lin, C.P. Huang, W. Li, C. Ni, S. Ismat Shah, Yao-Hsuan Tseng, *Appl. Catal. B* 68

- (2006) 1–11.
- [54] K. Momma, F. Izumi, *J. Appl. Crystallogr.* 41 (2008) 653–658.
- [55] J.C. Bunzli, C. Piguet, *Chem. Soc. Rev.* 34 (2005) 1048–1077.
- [56] A.V. Naumkin, A. Kraut-Vass, S.W. Gaarenstroom, C.J. Powell, NIST X-ray Photoelectron Spectroscopy Database 20. Version 4.1, (2012) <http://srdata.nist.gov/xps/>.
- [57] Y.A. Teterin, A.Y. Teterin, *Russian Chem. Rev.* 71 (2002) 347–381.
- [58] J. Reszczynska, T. Grzyb, J.W. Sobczak, W. Lisowski, M. Gazda, B. Ohtani, A. Zaleska, *Appl. Catal. B* 163 (2015) 40–49.
- [59] C. Lazar, E. Burzo, M. Neumann, *J. Optoelectron. Adv. Mater.* 10 (2008) 780–782.
- [60] A. Bianconi, A. Kotani, K. Okada, E. Giorgi, A. Gargano, A. Marcelli, T. Miyahara, *Phys. Rev. B* 38 (1988) 3433–3437.
- [61] H. Ogasawara, A. Kotani, R. Potze, G.A. Sawatzky, B.T. Thole, *Phys. Rev. B* 44 (1991) 5465–5469.
- [62] M.D. Ulrich, J.E. Rowe, D. Niu, G.N. Parsons, *J. Vac. Sci. Technol. B* 21 (2003) 1792–1797.
- [63] Y. Ohno, *J. Electron Spectr. Relat. Phenom.* 165 (2008) 1–4.
- [64] G. Zhang, W. Jiang, S. Yu, *Mater. Res. Bull.* 45 (2010) 1741–1747.
- [65] M. Makarova, P. Bykov, J. Drahokoupil, M. Cernansky, Z. Dlabacek, A. Dejneka, L. Jastrabik, V. Trepakov, *Mater. Res. Bull.* 47 (2012) 1768–1773.
- [66] C. Kittel, *Introduction to Solid State Physics*, Wiley, New York, 2005.
- [67] M. Matsunami, T. Hashizume, A. Saiki, *Arch. Metall. Mater.* 60 (2015) 941–944.
- [68] C.H. Wen, S.Y. Chu, Y.Y. Shin, C.T. Lee, Y. Der Juang, *J. Alloys Compd.* 459 (2008) 107–112.
- [69] A. Cybula, G. Nowaczyk, M. Jarek, A. Zaleska, *J. Nanomater.* 2014 (2014) (9 pages).
- [70] B. Zielińska, R.J. Kalenczuk, *Int. J. Photoenergy* 2012 (2012) (7 pages).
- [71] R. Abe, M. Higashi, Z. Zou, K. Sayama, Y. Abe, *Chem. Lett.* 33 (2004) 954–955.
- [72] M. Uno, A. Kosuga, M. Okui, K. Horisaka, *J. Alloys Compd.* 400 (2005) 270–275.
- [73] Y. Yaoguang, C. Gang, Z. Yansong, H. Zhonghui, *J. Rare Earth* 33 (2015) 453–462.
- [74] K. Maeda, *Phys. Chem. Chem. Phys.* 15 (2013) 10537–10548.